ELSEVIER

Formation of todorokite from vernadite in Ni-rich hemipelagic sediments

Sabine Bodeï [a], Alain Manceau [b,*], Nicolas Geoffroy [b],
Alain Baronnet [c], Martine Buatier [a]

[a] *Département de Géosciences, Université de Franche-Comté, 16 Route de Gray, 25030 Besançon, France*
[b] *Environmental Geochemistry Group, LGIT, University J. Fourier and CNRS, BP 53, F-38041 Grenoble Cedex 9, France*
[c] *CRMCN, F-13288 Marseille 09, France*

Abstract

Todorokite is considered to form from vernadite in nature and commonly concentrates nickel. However, this mineralogical transformation has never been imaged nor explained mechanistically, and its effect on the uptake of nickel has never been quantified at the molecular-level. We have characterized these reactions at the macroscopic, microscopic, nanoscopic and atomic scales in a marine manganese concretion by combining transmission electron microscopy, electron and X-ray microprobe analysis, powder and micro X-ray diffraction, and Mn and Ni K-edge EXAFS spectroscopy. The concretion was collected during the Ticoflux II expedition near the Nicoya Peninsula, Costa Rica, and is representative of Mn deposits in hemipelagic sediments. It consists of 5 to 25 μm aggregates, shaped like sea-urchins, with a core of 7Å-vernadite (1.0 wt% Ni), a rim of 10Å-vernadite (3.8 wt% Ni), and an outermost region of todorokite fibers (1.9 wt% Ni) that extend outwards. The crystallites of 7Å-vernadite are single- to bi-layered, with hexagonal layer symmetry ($a = b = 2.83$ Å), and an average structural formula of $Mg^{2+}_{0.161}Ca^{2+}_{0.010}K^{+}_{0.016}[Mn^{4+}_{0.902}Vac_{0.083}Ni^{2+}_{0.015}]O_2 \cdot nH_2O$. The crystallites of 10Å-vernadite contain 10 to 20 layers semi-coherently stacked in the ab plane and uniformly separated in the $[001]$ direction by $\sim$9 Å due to the intercalation of hydrated Mg^{2+} cations. The average structural formula of 10Å-vernadite is $Mg^{2+}_{0.187}Ca^{2+}_{0.016}K^{+}_{0.013}[Mn^{4+}_{0.864}Vac_{0.074}Ni^{2+}_{0.062}]O_2 \cdot nH_2O$ if the layers contain vacancy sites, or alternately $Mg^{2+}_{0.202}Ca^{2+}_{0.018}K^{+}_{0.014}[Mn^{4+}_{0.613}Mn^{3+}_{0.320}Ni^{2+}_{0.067}]O_2 \cdot nH_2O$, if they contain Mn^{3+}. The average formula of todorokite is $Mg^{2+}_{0.178}Ca^{2+}_{0.013}K^{+}_{0.019}[Mn^{4+}_{0.612}Mn^{3+}_{0.356}Ni^{2+}_{0.032}]O_2 \cdot nH_2O$.

A genetic model is proposed based on combining these new data with previously published results. The thermodynamically unstable 7Å-vernadite transforms via dissolution-recrystallization to semi-ordered Mg-rich 10Å-vernadite. Nickel is released from dissolved biogenic silica or reduced organic matter, and taken up mainly in the Mn layer of 10Å-vernadite. Interlayer magnesium serves as a template to the further topotactic transformation of 10Å-vernadite to todorokite. The dimension of the todorokite tunnels in the $[001]$ direction is uniform and determined by the size of the hydrated Mg^{2+} ion (8.6 Å). The tunnel dimension in the $[100]$ direction depends on the density of Mg^{2+} in the interlayer and the superstructure of the phyllomanganate layer. If the parent phyllomanganate contains high amounts of Mg^{2+} (i.e., high layer charge), or Mn^{3+} and Mn^{4+} cations ordered following the Mn^{3+}–Mn^{4+}–Mn^{4+} sequence as in synthetic triclinic birnessite, then the tunnel dimension is ideally 3×3 octahedral chain widths in both crystallographic directions. Otherwise, the tunnel dimension is incoherent in the $[100]$ direction (i.e., $T(3,n)$ tunnel structure), as has been observed in all natural todorokites. Natural todorokite is defective because the precursor natural phyllomanganates either have a layer charge deficit below 0.33e per octahedral site, or rarely are triclinic birnessite. The abundance of Mg in seawater and its key role in converting phyllomanganate to tectomanganate with $T(3,n)$ tunnel structure explain why todorokite is common in marine ferromanganese oxides, and

---

* Corresponding author.
  E-mail address: Alain.Manceau@obs.ujf-grenoble.fr (A. Manceau).

seldom present in terrestrial environments. The topotactic phase transformation described here is the only known route to todorokite crystallization. This implies that all natural todorokites may be authigenic because they are formed *in situ* from a phyllomanganate precursor.

1. INTRODUCTION

The tectomanganate todorokite and the turbostratic phyllomanganate vernadite often are associated in ferromanganese oxides from marine (Burns and Burns, 1978a,b; Corliss et al., 1978; Siegel and Turner, 1983; Usui et al., 1986, 1997; Usui and Glasby, 1998; Banerjee et al., 1999; Buatier et al., 2004; Takahashi et al., 2007) and terrestrial environments (McKeown and Post, 2001). The two manganates generally are mixed on a fine scale that cannot be resolved either optically or by electron microprobe (Usui et al., 1997; Banerjee et al., 1999). Despite the lack of direct evidence, todorokite has long been suspected to form from vernadite (Burns and Burns, 1978b). Three varieties of vernadite can be distinguished on the basis on chemical and diffraction data: 7Å-vernadite, 10Å-vernadite, and Fe-vernadite (Ostwald, 1984; Varentsov et al., 1991; Manceau et al., 2007a,b). The first two varieties are one-water layer (7Å) and two-water layer (10Å) hydrates of the same type of mineral, each of which consists of octahedral Mn layers stacked vertically with a constant separation, but without three-dimensional (3D) periodicity. Their diffractograms have basal reflections at 7Å (001) and 3.5 Å (002) for the 7Å varieties and 10 Å (001) and 5 Å (002) for the 10Å varieties. Two asymmetrical *hk0* reflections (or *hk* bands) at 2.40–2.45 and 1.41–1.42 Å are detected at higher diffraction angles, but no *hkl* reflections occur because the layers are stacked randomly without translational periodicity along the *c* direction (no 3D ordering, Giovanoli and Bürki, 1975; Holland and Walker, 1996; Drits et al., 1997; Villalobos et al., 2006). In contrast, the diffracting crystallites of Fe-vernadite are typically single layers and, therefore, do not have basal nor *hkl* reflections, only *hk0* reflections. In the last varieties, parallel Mn layers can be disrupted by epitaxial intergrowths of Fe oxide nanoparticles (Burns and Burns, 1975, 1979; Golden et al., 1988; Manceau and Combes, 1988; Varentsov et al., 1991; Manceau et al., 1992). In deep-sea ferromanganese nodules, todorokite typically is associated with 10Å-vernadite in Mn-rich layers that alternate with Fe-rich layers made of Fe-vernadite (Siegel and Turner, 1983; Banerjee et al., 1999; Hatta et al., 1999). Therefore, if todorokite forms from vernadite, it appears to be derived from the 10Å varieties. This hypothesis is corroborated experimentally by the formation of todorokite from buserite, a 3D-ordered analog to 10Å-vernadite (Giovanoli et al., 1975; Golden et al., 1986, 1987; Shen et al., 1993; Feng et al., 1995, 2004; Ching et al., 1999; Luo et al., 1999). Today, this is the only known route to synthesizing todorokite.

Vernadite and todorokite are of potential economic interest because they often contain several tenths to more than one weight percent of Co, Ni, Cu and other strategic metals, including platinum group metals and Rare Earth Elements (REE, Glasby, 2006). Therefore, a fundamental knowledge of the vernadite to todorokite transformation is critical to understanding the partitioning and distribution of trace metals in oceanic sediments for prospective exploration and mining activities. In metalliferous ferromanganese oxides, Ni is associated with 10Å-vernadite and todorokite, not Fe-vernadite (Burns and Burns, 1978b; Moore et al., 1981; Lei and Boström, 1995; Usui et al., 1997; Banerjee et al., 1999). Early investigators concluded that Ni is associated specifically with todorokite (Burns and Burns, 1977, 1978b), but at this time 10Å-vernadite was unknown and the X-ray reflections with *d* spacings of $\sim$10 and $\sim$5 Å were attributed to todorokite. Later, Ni was shown by electron microscopy to be concentrated in an unidentified 10-Å phase coexisting with todorokite in a Pacific nodule (Siegel and Turner, 1983). More recent investigations have not been compelling because analytical tools lacked spatial resolution (Banerjee et al., 1999).

The question remains as to how Ni is incorporated structurally in 10Å-vernadite and todorokite. In todorokite, Ni is thought to be substituted for Mn in octahedral sites at the edges of the triple chains (Fig. 1, Post and Bish, 1988). Phyllomanganates offer more possibilities than tectomanganates for Ni uptake because they have a larger variety of chemical (layer vacancy, mixed valence) and structural (stacking faults, low dimensionality) defects. Also, the density of defects is higher than in tectomanganates, which means that phyllomanganates can incorporate more Ni, and in general trace metals, per unit weight. For example, the vernadite-like Mn oxide produced by *Pseudomonas putida* (layer formula $[Mn_{0.833}^{4+}Vac_{0.167}]O_2$) has a layer charge deficit ($\sim$850 meq/100 g) eight to nine times higher than that of the smectite clay montmorillonite ($\sim$100 meq/100 g) (Villalobos et al., 2006). The negative layer charge originating from the deficit of Mn^{4+} in the octahedral sheet can be balanced partly or totally by a substitutional cation at the vacant site (Vac) or an interlayer cation above it. The first compensation mechanism was described for Co and Ni (Manceau et al., 1997, 2007a,b), and the second for Ni, Zn, Pb, and Cu (Silvester et al., 1997; Morin et al., 1999; Matocha et al., 2001; Manceau et al., 2002a, 2007b). Interlayer cations may also occupy the empty tetrahedral cavity formed by three edge-sharing Mn octahedra, for example when the layer charge is due to Mn^{3+} for Mn^{4+} substitution (Drits et al., 2002; Lanson et al., 2002a). Metal sorption on edge sites can be significant when the lateral dimension of the manganese layer is nanometric, as is mostly the case for natural phyllomanganates (Morin et al., 2001; Villalobos et al., 2005; Takahashi et al., 2007). Yet another mechanism of Ni uptake is the insertion of a $Ni(OH)_2$ layer in the interlayer of a phyllomanganate, yielding a hybrid structure, with a *c* dimension of $\sim$10Å called asbolane (Chukhrov et al., 1980b,c; Manceau et al., 1987, 1992).
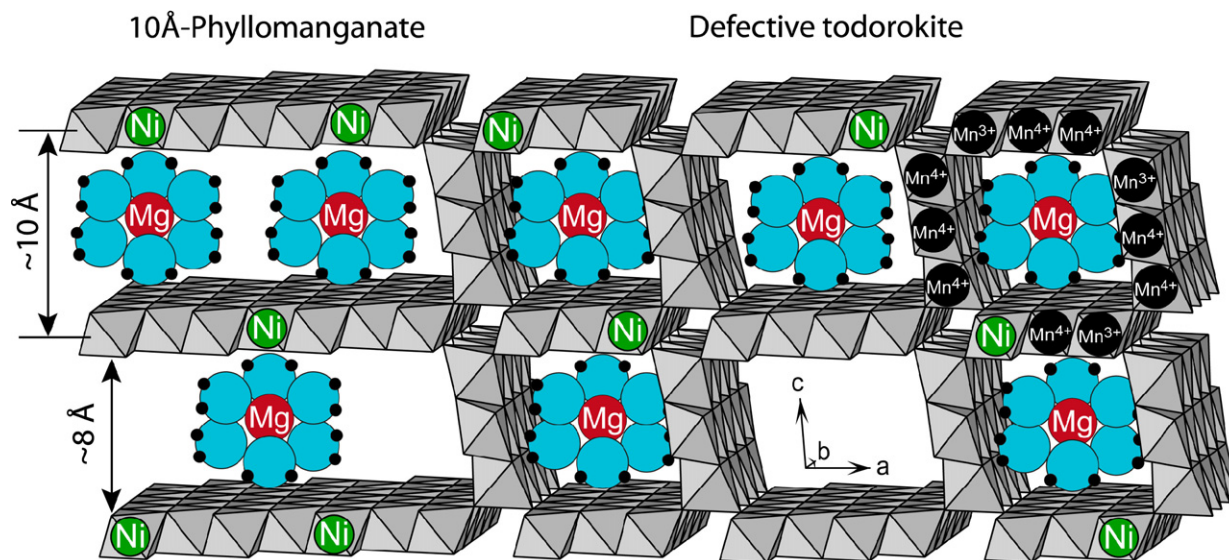
Fig. 1. Schematic representation of the topotactic transformation of 10Å-phyllomanganate to todorokite. Tetravalent manganese cations likely occupy the central and edge sites of the triple chains from the todorokite framework, and the larger trivalent manganese and divalent nickel cations the edge sites, exclusively (Post and Bish, 1988; Post et al., 2003).

The goals of our study were to understand how todorokite forms and how Ni partitions in manganese oxides from hemipelagic sediments. The sample is from a buried hydrothermal manganese deposit discovered during the Ticoflux II expedition in 2002 (Fisher et al., 2003). These hydrothermal deposits are considered to be largely stable in deep marine sediments and, therefore, are regarded as palaeoceanographic indicators for past manganese mineralization (Usui and Nishimura, 1992; Harris et al., 2004). Here, evidence for post-depositional mineralogical and geochemical transformation have been obtained using a combination of imaging, analytical, mineralogical and spectroscopic techniques having high spatial or structural resolution. Specifically, the micromorphology of the manganese concretions was imaged by transmission electron microscopy (TEM), and their mineralogy determined by high-resolution TEM (HRTEM), selected area electron diffraction (SAED), powder and micro X-ray diffraction (XRD, μ-XRD), and Mn K-edge extended X-ray absorption fine structure (EXAFS) spectroscopy. The chemical composition of the Mn phases was obtained by electron-probe energy dispersive spectroscopy (EDS) and synchrotron-based X-ray micro-fluorescence (μ-XRF), and the crystal chemistry of Ni was determined by Ni K-edge EXAFS spectroscopy.

2. MATERIALS AND METHODS

2.1. Sample

Sample 50GCC was collected in a non-indurated Mn oxide layer (maximum thickness of 6 cm) at 3150 m water depth and 100 cm below the sediment surface on the northwestern slope of the Dorado basaltic outcrop. This 100 m high active mount is located offshore Costa Rica near the Nicoya Peninsula (9°05.044N–87°05.929W). The sample was stored at 4 °C until further characterization. Part of the sample was air-dried and crushed in an agate mortar. From this part the < 20 μm fraction was extracted by sieving for X-ray diffraction and chemical and spectroscopic analyses. An unperturbed fraction was impregnated in a Spurr resin following the methods of Elsass et al. (1998), cut with a diamond knife on an ultramicrotome, and mounted on carbon-coated Cu grids for electron microscopy. This resin has no Ni, as indicated by EDS and μ-XRD analysis of a blank sample.

2.2. Methods

Powdered sample was ignited at 1000 °C with lithium tetraborate, then dissolved in a glycolated solvent for chemical analysis (Samuel et al., 1985). Major elements were analyzed by inductively coupled plasma-atomic emission spectrometry (ICP-AES, Jobin-Yvon JY 70), and trace elements, including rare-earths, by inductively coupled plasma-mass spectrometry (VG Plasmaquad PG2+). The precision on all analyses is 5%. Powder XRD patterns were recorded using a Bruker D5000 diffractometer equipped with a Kevex Si(Li) solid detector and CuKα radiation from 5° to 80° at a 0.04° 2θ interval, using a 60 s counting time per step. Two patterns were recorded, one from air-dried powder (Air-50GCC) and another from powder dehydrated in situ in vacuum (Vac-50GCC). For vacuum measurements, the sample was mounted in an Anton Paar TTK450 chamber evacuated to $\sim 10^{-4}$ hPa residual pressure with a Varian V70 turbo-molecular pump. The sample was equilibrated for 2 h at low pressure before collecting data. Micro-XRD, μ-XRF and Mn K-edge EXAFS data were recorded on the X-ray microprobe 10.3.2 at the Advanced Light Source (ALS), Berkeley (Marcus et al., 2004a). The μ-XRD patterns were recorded in transmission with a Bruker 6000 CCD binned to

1024 × 1024 pixels at 17 keV incident X-ray energy. The two-dimensional XRD patterns were calibrated with corundum (α-Al_2O_3) and integrated to one-dimensional patterns with the Fit2d code (Hammersley et al., 1996). The powder Mn-EXAFS spectrum was measured in transmission mode and is the average of eight scans collected at separate locations with a 7×16 μm^2 beam. The Ni-EXAFS spectrum from a homogenous powder was measured in fluorescence-yield mode with a wide beam (300×150 μm^2) on beamline FAME at the European synchrotron radiation facility (ESRF), Grenoble (Proux et al., 2006). Details on the experimental procedures can be found elsewhere (Manceau et al., 2002b, 2007a). EXAFS data were analyzed by standard procedures (Teo, 1986).

The TEM observations and analyses were performed with a Jeol 1260 microscope operating at 120 kV (CCME laboratory, Université de Franche Comté, Besançon) and a Philips CM30 operating at 300 kV and equipped with an energy dispersive X-ray detector (CCM laboratory, Université de Lille 1). The EDS measurements were carried out in STEM mode using a square window of about 20 nm. Micro-chemical analyses were quantified by the method of Cliff and Lorimer (1975) using the following standards: natural andalusite for Al, natural jadeite for Na, natural wollastonite for Ca, synthetic forsterite for Mg, and synthetic fayalite for Fe. The HRTEM observations were performed on a JEOL 3010 microscope operating at 300 kV (CRMCN laboratory, Marseille). This microscope is equiped with objective pole pieces insuring a 2.1 Å point-to-point resolution of the images. Mechanical and charge drifts of the microtomed preparations were minimized by waiting for stabilization under low electron current, using low magnifications (140,000× to 300,000×), and then scanning the film sample at high-resolution (greater than 2000 dpi). After isolating single particles with a suitable objective aperture, the selected-area electron diffraction (SAED) patterns were recorded on overexposed films to enable the recording of weak diffuse streaks in addition to main diffraction spots.

3. RESULTS AND INTERPRETATIONS

3.1. Chemical composition

The sample is rich in Ni (6333 mg/kg), and to a lesser extent in Cu (978 mg/kg) and Co (765 mg/kg, electronic annex). Its metalliferous character suggests a hydrogenetic or diagenetic origin, not a hydrothermal origin (Usui et al., 1997; Wen et al., 1997). The Mn/Fe ratio is about 17 (Table 1). Typically, the Mn/Fe ratio increases from about 1 in hydrogenetic to about 5–10 in diagenetic to 20 and higher in hydrothermal deposits (Takahashi et al.,

2007); thus, the source of manganese for 50GCC is clearly not hydrogenetic. Consistent with this interpretation, the upper part of the sediment core had less Mn (electronic annex). The REE values for 50GCC, normalized to those of the Post-Archean Australian Shale (McLennan, 1989), and deep seawater (Piepgras and Jacobsen, 1992), show a pattern intermediate between those of high-temperature hydrothermal and diagenetic deposits, and similar to those of low-temperature hydrothermal or sub-oxic diagenetic deposits (Usui et al., 1997; Takahashi et al., 2007) (Fig. 2). The mixed diagenetic—low-temperature hydrothermal genetic nature of 50GCC also is supported by the evolution of REE patterns with depth in the sediment core. Ten samples analyzed from between 12 and 124 cm below the sediment surface exhibit typical hydrothermal REE patterns characterized by a pronounced negative Ce anomaly and a marked enrichment in heavy REEs relative to light REEs, when normalized to PAAS (Fig. EA-1, Elderfield and Greaves, 1981; German et al., 1990; Hodkinson et al., 1994; Kuhn et al., 1998). However, the three deepest samples (100, 110 and 124 cm) are more depleted in Ce than the others (12, 26, 30, 38, 54, 58 and 70 cm). The higher abundance of Ce towards the surface suggests that the sediment composition was influenced by seawater. In contrast, the deeper samples (e.g., 58, 70, 110 and 124 cm) are in general richer in heavy REEs than the upper samples, as shown by the more asymmetrical shape (i.e., less flat) of their REE patterns. The same change in pattern shape also appears between hydrothermal and diagenetic/hydrogenetic Mn oxides (Fig. 2a). Thus, the 50GCC concretion is regarded as a low-temperature hydrothermal deposit with a composition modified by diagenesis: Mn is considered to have been provided mostly by low-temperature hydrothermal fluids, whereas the enrichment of trace elements (Ni, Cu, Co) in Mn oxides likely results from seawater-sediment interaction since they have a biogenic origin in oceanic sediments and are depleted in hydrothermal Mn deposits (Usui et al., 1997; Wen et al., 1997). The formation of Mn deposits by diffuse seepage of hydrothermal water is common in venting sites near submarine volcanic regions (German et al., 1991; Cronan and Hodkinson, 1997; Kuhn et al., 1998).

3.2. Mineralogy

3.2.1. XRD

The XRD pattern from the sample powder contains sharp peaks from well-crystallized mineral species and broad maxima at ~9.5–9.6, ~4.8, ~2.4 and ~1.40 Å from Mn oxides (Fig. 3a). Sharp peaks match the prominent powder diffraction lines of quartz, albite, apatite, halite, and zeolite (mostly phillipsite and clinoptilolite), and the broad maxima those from todorokite. Zeolite is a common

Table 1
Chemical composition by wet chemistry

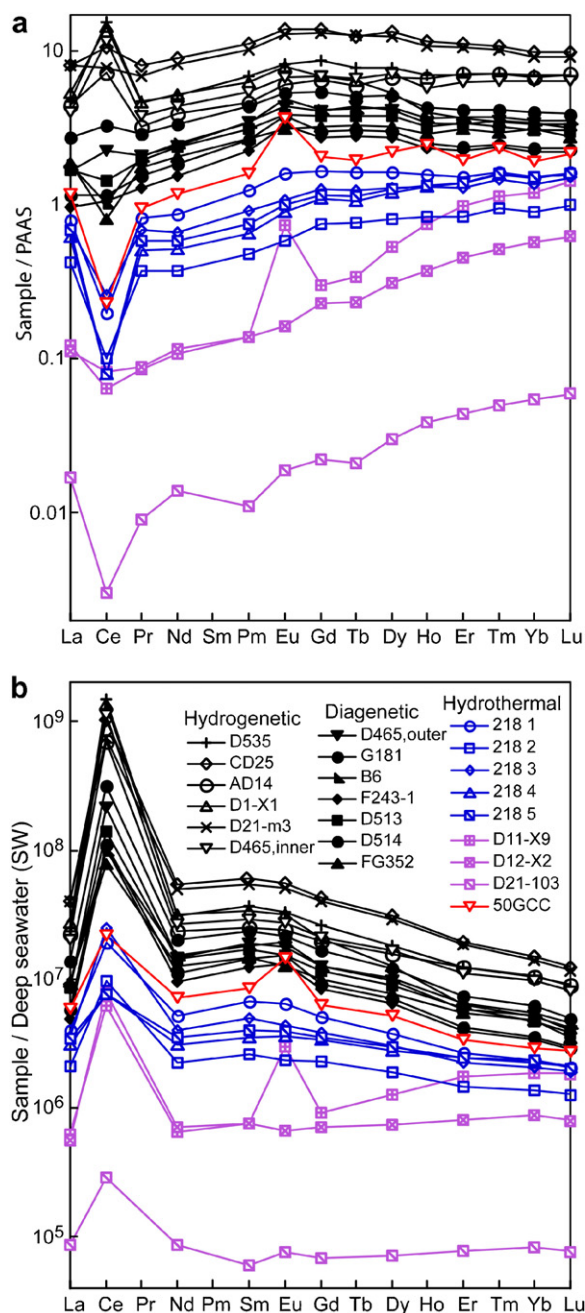| SiO$_2$ (%)	Al$_2$O$_3$ (%)	MgO (%)	CaO (%)	Fe$_2$O$_3$ (%)	MnO (%)	TiO$_2$ (%)	Na$_2$O (%)	K$_2$O (%)	P$_2$O$_5$ (%)	NiO (mg/kg)	CuO (mg/kg)	Co$_2$O$_3$ (mg/kg)	LOI (%)	Sum	Mn/Fe (at.)
15.1	4.7	3.9	4.0	2.8	42.3	0.2	1.5	0.3	1.9	8059	1224	1076	18.7	96.4	16.73

LOI, loss on ignition.

Fig. 2. REE patterns normalized to abundances in Post-Archean Australian Shale (PAAS, McLennan, 1989) (a), and deep seawater (SW, Piepgras and Jacobsen, 1992) (b), for 50GCC and samples data reported in Usui et al. (1997) and Takahashi et al. (2007).

authigenic constituent of marine sediments (Halbach et al., 1975; Burns and Burns, 1978a; Usui and Ito, 1994), and is believed to form from the hydration of volcaniclastic material in seawater (Riley and Chester, 1971; Cronan, 1974; McCoy and Sancetta, 1985). Dehydrating the sample in vacuum decreased the d spacing of most zeolite peaks and the position and intensity of the maxima at 9.5–9.6 and 4.75–4.80 Å (Fig. 3b). The modification of the two last peaks suggests the presence of phyllomanganate (i.e.,

10Å-vernadite) whose interlayer region is reduced when the partial vapor pressure is diminished (Yoshikawa, 1991). Confirmation was obtained by μ-XRD.

Fifteen μ-XRD patterns and μ-XRF spectra were recorded in air at points-of-interest (POIs) on finely dispersed powder with a 5×5 μm^2 X-ray beam (Fig. EA-2 and EA-3). Three types of μ-XRD patterns were identified (Fig. 3a). The POI-1 type of pattern was collected at spots with low Ni concentrations (Fig. 3c). It has a broad and weak hump at ~7 Å, and two maxima at ~2.455 ± 0.005 and ~1.415 ± 0.005 Å asymmetrical on their high 2θ-angle sides (i.e., low d-spacing). The two last maxima correspond to 20,11 and 02,31 bands, choosing a C-centered layer cell (Villalobos et al., 2006). The asymmetrical scattering profile, combined with the 7 Å peak and weak intensity of the Fe Kα and Kβ fluorescence lines (Fig. 3c), are diagnostic of 7Å-vernadite (Manceau et al., 2007a,b). The $d(20,11)/d(02,31)$ ratio is ~$\sqrt{3}$, which indicates that the Mn layers have hexagonal symmetry with $a = b = 2.83$ Å (Drits et al., 1997). The low value of the layer-cell dimension means that the layers do not contain detectable Mn^{3+} (Manceau et al., 1997). In comparison, synthetic hexagonal birnessite (the 3D ordered analog to 7Å-vernadite) equilibrated at pH 4 has 13% Mn^{3+} in the layer and a b parameter of 2.848 Å (HBi,H$_{0.33}^+$Mn$_{0.043}^{2+}$Mn$_{0.123}^{3+}$(Mn$_{0.722}^{4+}$ Mn$_{0.111}^{3+}$Vac$_{0.167}$)O$_2$(OH)$_{0.013}$, Lanson et al., 2000) while lithiophorite (Al$_{0.67}$Li$_{0.32}$)(Mn$_{0.68}^{4+}$Mn$_{0.32}^{3+}$)O$_2$(OH)$_2$, which contains 32% layer Mn^{3+} (Yang and Wang, 2003; Manceau et al., 2005), has $a = b = 2.925$ Å (Post and Appleman, 1994). The POI-2 type of pattern was recorded at low to medium Ni spots. It has diffraction maxima at ~9.52 and ~4.78 Å, which may correspond to either todorokite or 10Å-vernadite. However, the peak at ~2.4 Å has the same composite shape as that for todorokite, and the position of the maxima in the 2.40–1.42 Å interval match those from todorokite, indicating that this is the major species at POI-2. The POI-3 pattern is representative of the high Ni spots. It has the same reflections as POI-2, but a distinct scattering profile at ~2.4 Å: the reflection at 2.40 Å that comes from todorokite is less intense and the third reflection from the composite band at 2.35 Å is faint. Therefore, the Ni-rich spots have less todorokite and more 10Å-vernadite, suggesting that Ni is more abundant in the vernadite species. The high Ni 10Å-crystallites are also those which contain the highest number of stacked layers because basal reflections were systematically stronger in the presence of Ni. On the basis of XRD calculations performed on phyllomanganates with variable crystallinity, the average number of layers in the diffracting crystallites may be as low as 2–3 in low Ni, and as large as 8–10 in high Ni, crystallites (Usui and Mita, 1995; Manceau et al., 1997; Lanson et al., 2002a; Villalobos et al., 2006). It will be shown below that these numbers are realistic based on HRTEM observations. In summary, 50GCC contains todorokite and two populations of vernadite, a high Ni two-water hydrate (10Å-vernadite) and a low Ni one-water hydrate (7Å-vernadite).

3.2.2. Mn EXAFS

The proportions of todorokite and vernadite in the bulk sample were determined by Mn-EXAFS spectroscopy. Nei-
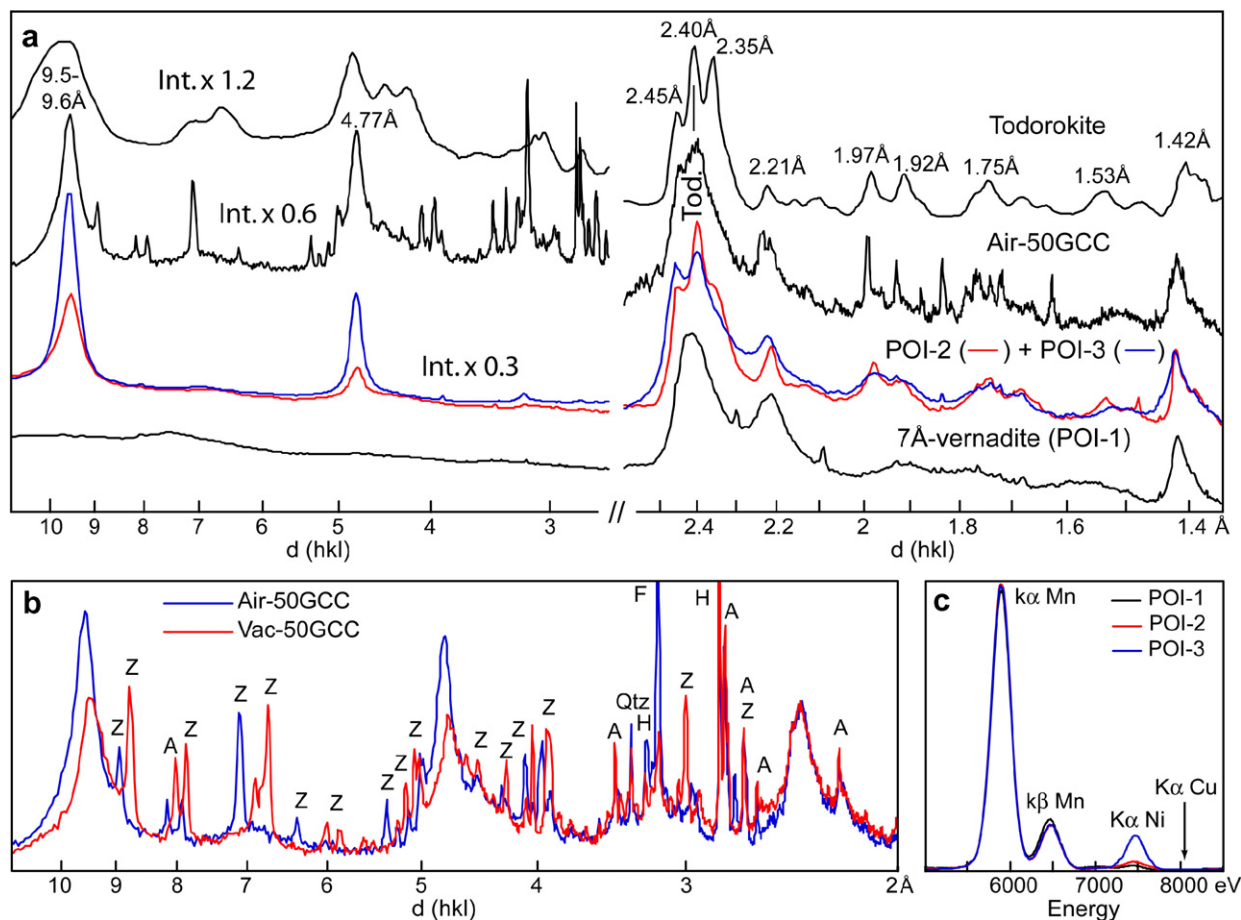
Fig. 3. X-ray diffraction patterns (a and b) and X-ray microfluorescence spectra (c) of 50GCC. A, apatite; F, feldspar; H, halite; Qtz, quartz; Z, zeolite. The diffraction maximum at 2.40 Å in the sample is due to todorokite. In (a), the pattern in red has been collected at POI-2 (high todorokite, low 10Å-vernadite), and the pattern in blue at POI-3 (high 10Å-vernadite, low todorokite). The diffracted intensities are scaled.

ther the spectrum from the todorokite nor the *c*-disordered hexagonal phyllomanganate references (dBi, $Na_{0.24}$ $(H_2O)_{0.72}$ $(Mn^{4+}_{0.94}Vac_{0.06})O_2$, Marcus et al., 2004b; Villalobos et al., 2006), optimally reproduced the data (Fig. 4a and b), in agreement with the XRD results. Clear differences are observed in the [7.0–9.5 $Å^{-1}$] indicator region (Marcus et al., 2004b), which is known to be sensitive to the amount and ordering of Mn^{4+} and Mn^{3+} in the manganese layer of phyllomanganate, and to the dimension of the tunnel in tectomanganate (Manceau and Combes, 1988; Manceau et al., 2002b, 2004, 2005; McKeown and Post, 2001; Gaillot et al., 2003). The optimized fit to the 50GCC spectrum was obtained with a combination of $55 \pm 10\%$ todorokite + $45 \pm 10\%$ phyllomanganate (dBi, Fig. 4c). Other phyllomanganate references having Mn^{3+} for Mn^{4+} layer substitutions (e.g., triclinic birnessite, Lanson et al., 2002b, and lithiophorite) or vacant Mn layer sites capped by interlayer Mn (e.g., HBi hexagonal birnessite, Silvester et al., 1997) yielded poorer matches to the data (Fig. EA-4).

3.2.3. TEM

Seen under TEM, the sample consists of aggregates 5 to 25 μm in diameter with a sea urchin-like external morphology (Fig. 5a). The innermost parts of the concretions have a disordered texture composed of entangled and distorted veil-like particles with diffuse edges and limited thickness (Fig. 5b). The particles are ~0.2 μm long and ~6–7 nm thick, on average. Their selected area electron diffraction pattern (SAED) shows only two diffraction rings of constant intensities along their perimeters with *d*-lattice spacings of 2.4 and 1.4 Å. Thus, core particles have the morphology and diffraction features typical of nanometer-sized, turbostratic vernadite (Chukhrov et al., 1979b, 1987; Manceau et al., 1992).

Particles from the outer regions have stronger electron contrast and larger size with a typical length of 0.3 μm and thickness of 40 nm (Fig. 5c). The evolution of particle size from the core to the rim is progressive and irregular. Outer particles also show diffraction rings at 2.4 and 1.4 Å, but with brighter areas separated by 60°. The variations of intensities along the ring perimeters indicate a mixture of semi-coherent and turbostratic stacks of hexagonal layers. But, we cannot conclude from electron diffraction alone, if the two types of diffracting units are interstratified in the same crystallites or are physically segregated in a mixture (Ferrage et al., 2005; Manceau et al., 2007a). We can answer this question by viewing particles in cross-section perpendicular to the layers at high-resolution. For example, the thick particle imaged in Fig. 6a contains four crystallites that are slightly twisted along the [0 0 1]
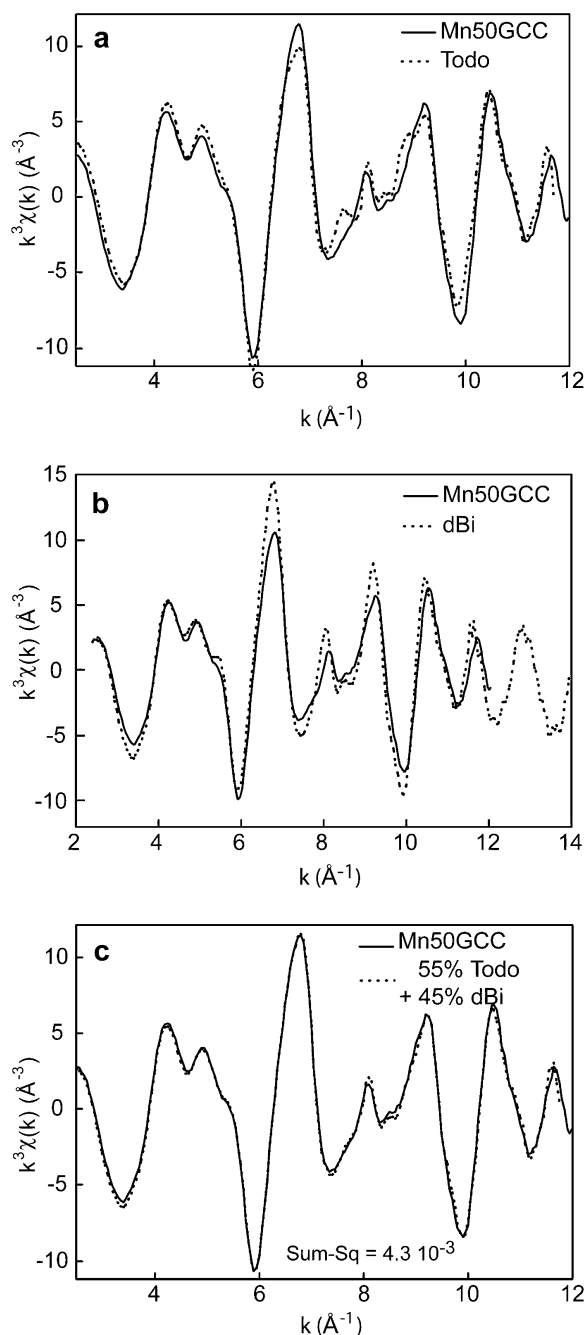
Fig. 4. Manganese K-edge EXAFS spectrum of 50GCC (solid line) compared to two reference spectra (a, todorokite; b, c-disordered hexagonal phyllomanganate) and least-squares fit with a combination of the two reference spectra (c). Sum-sq is the squares of the residuals, normalized to the sum of the squares of the data values.

direction, which misalignment explains the curved shape of particles at intermediate resolution (Fig. 5c). The layer separation within each crystallite is constant at 9 Å, consistent with the SAED pattern from a single crystallite taken perpendicular to the c direction that shows sharp spots separated by 9 Å (Fig. 6a, inset). Thus, successive layers in individual crystallites should have their a and b axes mostly oriented in the same directions, or rotated by about ±120°,

otherwise the SAED pattern from Fig. 5c would not have a pseudo-hexagonal symmetry. Therefore, the diffuse scattering between the six brightest spots of each ring partly originates from the disruption of layer coherence at particle boundaries, and perhaps also from stacking faults within crystallites. Since the 10Å-vernadite crystallites are semi-ordered three-dimensionally, they could be designated also as defective hexagonal buserite or 10Å-birnessite (see Manceau et al., 2007a for a discussion on phyllomanganate nomenclature). The number of layers in the semi-ordered crystallites from the outermost portion of the concretion ranged from 10 to 20.

The elongated crystals radiating from the surface of the aggregates are 1.0 to 2.5 μm in length and 15 to 100 nm in width (Fig. 5d). The d-spacings of their hkl reflections match those from todorokite. No trilling pattern of fiber crystals twinned at 0°, 120° and 240° from each other was observed at low-resolution. High-resolution images of single fibers along the c* direction show tunnels whose width varies irregularly from double to quintuple manganese octahedral chains in the a direction (Fig. 6b). Diffraction patterns along the [0 0 1] zone axis of this area and other sample fragments showed intense substructure spots with pronounced streaks in the a* direction. These streaks result from the lack of periodic ordering of chain widths (Siegel and Turner, 1983). Occasionally, two sets of diffraction patterns rotated by 120° were observed by SAED at high-resolution (Fig. 6b, inset), indicating that twins occur on a fine scale and in two out of three possible crystallographic orientations. The distribution of tunnel sizes was imaged by viewing one todorokite crystal along the tunnel direction (i.e., the direction of fiber elongation). Electron-dense dark areas in Fig. 6c correspond to tunnel walls, and white areas to tunnel apertures. Tunnels have a constant triple-chain width along c and a variable width of three to five octahedra along a, confirming aperiodic intergrowth in this direction. Successive sequences do not always repeat in the c direction, since a 453 sequence changes to a 344 sequence, and a 53 sequence to 333. These disruptions are another source of disorder in the a direction. Fig. 6d shows a former vernadite crystallite which has been topotactically transformed to todorokite. Since the tunnel dimension is periodic along c and aperiodic along a, the spacing of the fringes can be used to deduce the crystallographic orientation of the initital vernadite platelet (Fig. 1). All these observations are consistent with previous HRTEM data on natural and synthetic todorokites (see e.g., Chukhrov et al., 1979a; Turner and Buseck, 1979, 1981; Turner et al., 1982; Siegel and Turner, 1983; Golden et al., 1986, 1987; Feng et al., 2004).

Sixty-two particles were analyzed by EDS (Table 2). Silicon and aluminum likely come from micro-fossil remains and phyllosilicates. All particles were rich in Mn ($66.31 < MnO < 69.90$ wt%) and low in Fe ($0.86 < Fe_2O_3 < 1.94$ wt%). As stated previously, the high Mn/Fe ratio is consistent with the mixed diagenetic/low-temperature hydrothermal origin of the ferromanganese deposit (Bonatti et al., 1976; Halbach et al., 1981; Usui and Nishimura, 1992; Usui et al., 1997; Takahashi et al., 2007). The high Mg content ($6.89 < MgO < 8.15$ wt%) is also indicative of
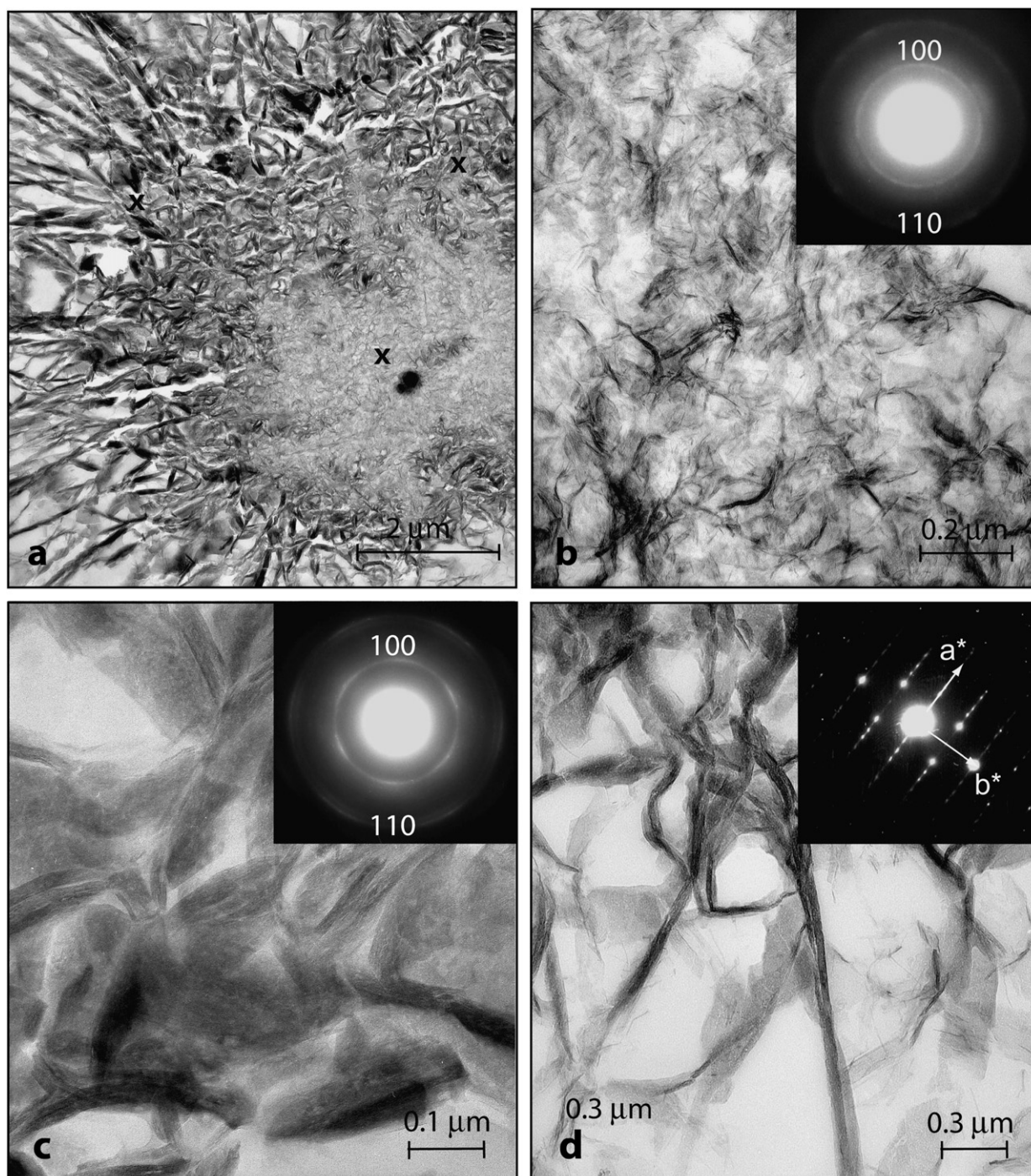
Fig. 5. Transmission electron microscope imaging and selected area electron diffraction of a manganese concretion. (a) Low-resolution image of a micronodule representing the morphology of Mn oxides in the non-indurated sediment layer. (b) 7Å-vernadite particles from the core. (c) 10Å-vernadite particles from the outermost region; (d) elongated todorokite crystals at the surface of the concretion. In (b), the two *hk*0 reflections are indexed with an hexagonal unit cell. The spotty diffraction pattern in (c) reveals a semi-periodic stack of layers (i.e., defective buserite crystals). The positions of the three regions shown in (b, c, and d) are marked with crosses in (a).

hydrothermal circulation (Usui et al., 1997). The largest variation in composition is seen for Ni. The 10Å-vernadite contains on average 3.8 wt% Ni, and todorokite and 7Å-vernadite one half (1.9%) and about one fourth (1.0%) this amount, respectively. The fraction of total Ni in each Mn phase cannot be calculated from these data alone because the proportions of 10- and 7Å-vernadite are unknown. However, since we know from Mn-EXAFS that the sample contains approximately equal amounts of phyllomanganate and tectomanganate, we can postulate that the two manganates each have about the same amount of nickel. In the oceanic nodule studied by Siegel and Turner (1983), the

unidentified 10Å-phase had 3.0 wt% Ni, and todorokite only 0.16% Ni. Here, Ni is more abundant and less partitioned.

From the chemical data (Table 2), two charge-balanced structural formulae can be calculated for each phylloman-ganate depending on whether the layer charge is attributed to Mn^{3+} for Mn^{4+} substitutions, as in triclinc birnessite (TcBi), or to Mn^{4+} vacancies, as in dBi.

7Å-vernadite : $Mg^{2+}_{0.175}Ca^{2+}_{0.011}K^{+}_{0.017}\left[Mn^{4+}_{0.628}Mn^{3+}_{0.355}Ni^{2+}_{0.017}\right]O_2 \cdot nH_2O$

7Å-vernadite : $Mg^{2+}_{0.161}Ca^{2+}_{0.010}K^{+}_{0.016}\left[Mn^{4+}_{0.902}Vac_{0.083}Ni^{2+}_{0.015}\right]O_2 \cdot nH_2O$

10Å-vernadite : $Mg^{2+}_{0.202}Ca^{2+}_{0.018}K^{+}_{0.014}\left[Mn^{4+}_{0.613}Mn^{3+}_{0.320}Ni^{2+}_{0.067}\right]O_2 \cdot nH_2O$

10Å-vernadite : $Mg^{2+}_{0.187}Ca^{2+}_{0.016}K^{+}_{0.013}\left[Mn^{4+}_{0.864}Vac_{0.074}Ni^{2+}_{0.062}\right]O_2 \cdot nH_2O$

In the first case, the 7Å-vernadite particles have as much as 35% Mn^{3+}, which is inconsistent with the layer dimen-sion determined by XRD. Therefore, these particles have

to have vacancies in an amount that does not exceed 0.083 per octahedral site. The higher amount of Ni in 10Å-vernadite relative to 7Å-vernadite is partly balanced by a decrease in the amount of vacancies, and possibly Mn^{3+}, such that the total layer charge is comparable in the two types of particles (0.358e and 0.42e per octahe-dral site, respectively). This layer charge is intermediate between those of dBi (0.24e) and HBi (0.78e), and much higher than that for 10Å-phyllomanganates in deep-sea nodules (0.17e, Usui, 1979). The sum of Ni and vacancies is much higher in the 10Å particles than in the 7Å par-ticles (0.136 vs. 0.098). Thus, this enrichment in Ni can-not be explained solely by its incorporation at preexisting vacancies in the 7Å particles. Consequently, the 7 to 10Å phase transformation does not occur com-pletely in the solid state, but must involve dissolution-recrystallization reactions.
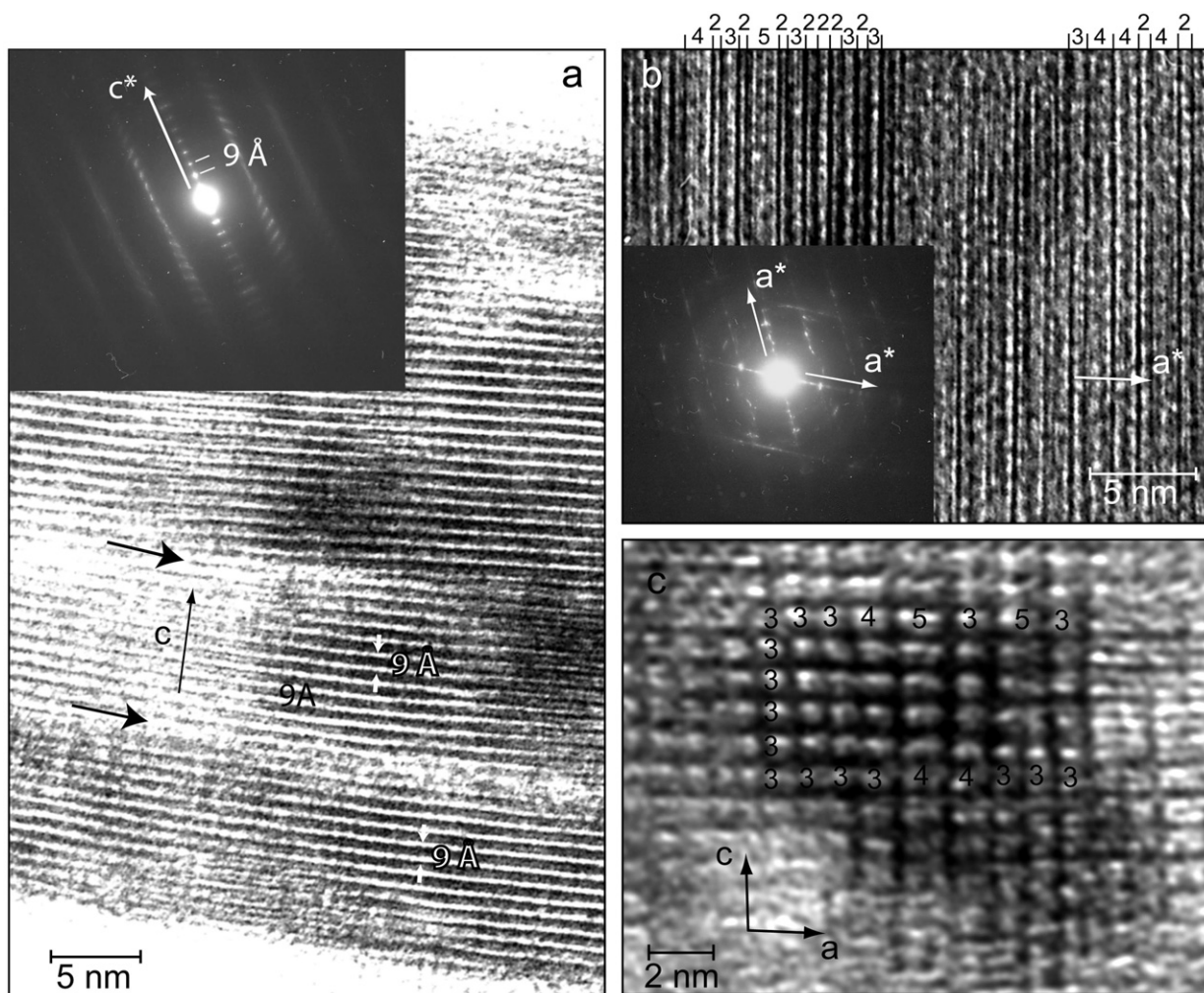

Fig. 6. (a) HRTEM image of a 10Å-vernadite thick particle from the outermost portion of a manganese concretion. The arrows point out the limits of a diffracting crystallite. Electron diffraction (inset) shows that the lattice fringe separation is constant and equal to 9 Å. (b) [001] zone axis HRTEM image of a todorokite fiber, showing variable chain widths in the a direction, and chain dislocations in the b direction. The SAED pattern has pronounced streaks along the two a^{*} directions rotated by 120° (twin crystals). (c) [010] zone axis HRTEM image showing coherent (c direction, vertical numbers) and incoherent (a direction, horizontal numbers) intergrowths of 3×3, 3×4 and 3×5 tunnel structures. (d) [010] zone axis HRTEM image of a former vernadite crystallite topotactically transformed to todorokite. The crystallite contains coherent and incoherent intergrowth domains.

Fig. 6 (*continued*)

Table 2
Chemical composition by EDS (wt%)

	7Å-vernadite[a]	10Å-vernadite[b]	todorokite[c]
Al_2O_3[d]	3.34 (1.12)	5.12 (1.47)	3.67 (1.42)
SiO_2[d]	14.12 (3.75)	12.19 (4.17)	12.62 (4.67)
Na_2O	0.50 (0.39)	0.17 (0.17)	0.44 (0.19)
MgO	6.89 (1.41)	8.15 (1.43)	7.29 (1.65)
K_2O	0.79 (0.24)	0.66 (0.31)	0.88 (0.29)
CaO	0.60 (0.33)	0.99 (0.50)	0.71 (0.16)
MnO	68.08 (3.98)	66.31 (6.29)	69.90 (5.26)
Fe_2O_3	1.94 (1.18)	0.86 (1.15)	0.89 (0.66)
NiO	1.23 (0.58)	5.01 (1.24)	2.45 (0.98)
Sum	97.49	99.46	98.85

Values in parenthesis are the standard deviations.
[a] Twenty-three particles analyzed.
[b] Fifteen particles analyzed.
[c] Twenty-four particles analyzed.
[d] Silicon and alumina are from siliceous and phyllosilicate impurities (Buatier et al., 2004).

The charge-balanced formula calculated for todorokite is

$$Mg_{0.178}^{2+}Ca_{0.013}^{2+}K_{0.019}^{+}\left[Mn_{0.612}^{4+}Mn_{0.356}^{3+}Ni_{0.032}^{2+}\right]O_2 \cdot nH_2O$$

It has a higher charge and is richer in Mg than the terrestrial specimens studied by Gutzmer and Beukes (2000):

$$Mg_{0.07}^{2+}Na_{0.06}^{+}Ca_{0.03}^{2+}K_{0.01}^{+}\left[Mn_{0.80}^{4+}Mn_{0.17}^{3+}Vac_{0.02}Fe_{0.01}^{3+}Al_{0.01}^{3+}\right]O_2 \\ \cdot 0.55H_2O$$

and Post et al. (2003):

$$Mg_{0.07}^{2+}Na_{0.07}^{+}Ca_{0.02}^{2+}K_{0.02}^{+}\left[Mn_{0.73}^{4+}Mn_{0.27}^{3+}\right]O_2 \cdot 0.7H_2O$$

The charge deficit introduced by divalent and trivalent cations in the framework sites (in brackets) is offset in the three cases mainly by Mg in tunnel sites. This confirms the role of Mg as an essential constituent in the todorokite structure. Interestingly, the charge deficit of the marine todorokite (0.42e/Mn) is the same as the 10Å-vernadite from which it derives.

3.3. Crystal chemistry of Ni

The local structure of Ni in 50GCC was evaluated initially by comparing the Ni-EXAFS spectrum to reference spectra described elsewhere (Manceau et al., 2002c, 2007a,b). The best match to the sample spectrum was obtained with natural Ni-containing vernadite from Lake

Baikal, the second-best with triclinic birnessite doped with 0.0044 Ni atom per Mn (NiTcBi), and the third-best with natural Ni-containing lithiophorite (NiLit, Fig. 7). Nickel
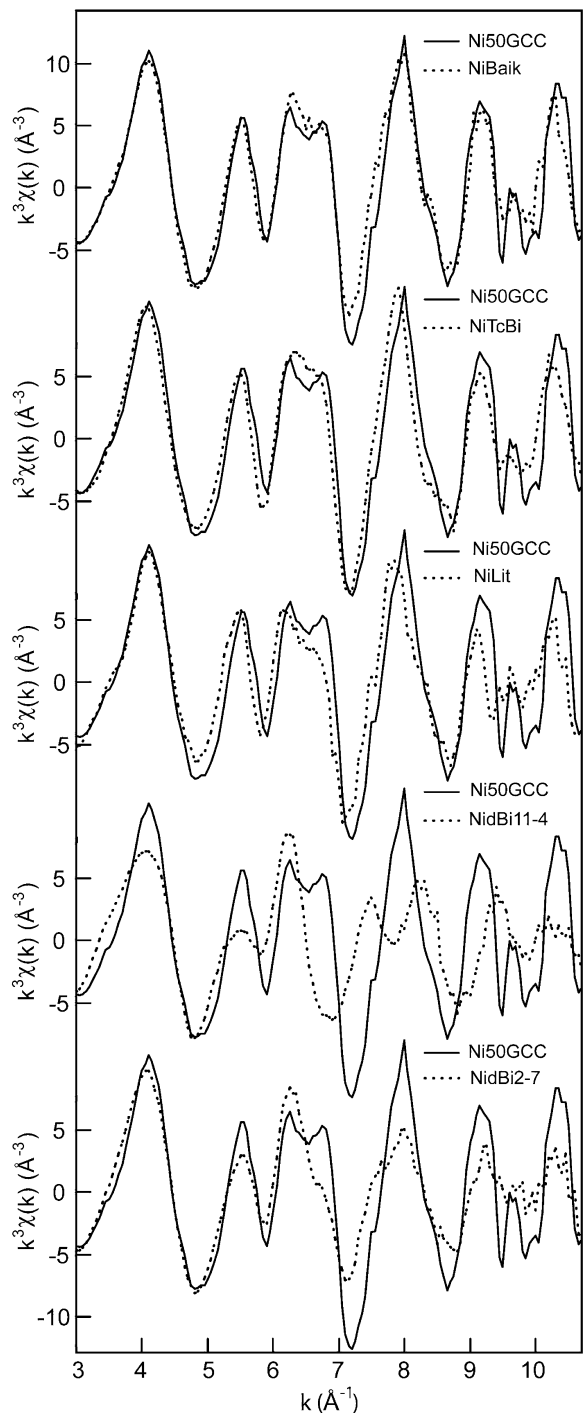

Fig. 7. Nickel K-edge EXAFS spectrum of 50GCC (solid line) compared to reference spectra (dotted line): natural Ni-containing 10Å-vernadite from Lake Baikal (NiBaik), Ni-substituted synthetic triclinic birnessite (NiTcBi, Ni/Mn = 0.0044), natural Ni-containing lithiophorite (NiLit), Ni sorbed on synthetic vernadite at pH 4 and Ni/Mn = 0.011 (NidBi11-4), and Ni sorbed on synthetic vernadite at pH 7 and Ni/Mn = 0.002 (NidBi2-7). The reference spectra are described in Manceau et al. (2002c, 2007a,b).

substitutes for Mn in the phyllomanganate layer of the three references, but it does not have the same short range order, as seen by the shifts in phase of the second and third EXAFS oscillations and of the imaginary parts of the Fourier transforms (FTs, Fig. 8). The Ni–Mn distances across octahedral edges (Ni–Mn(E) pairs) are longer in NiTcBi and NiLit as a result of the presence of $\sim$0.3 Mn^{3+} per Mn in the two phyllomanganates (Drits et al., 1997; Manceau et al., 2005). Thus, using nickel as a structural probe, EXAFS data confirm that the manganese layers of the vernadite crystallites in 50GCC have no detectable Mn^{3+}. The Ni–O and Ni–Mn(E) EXAFS distances (i.e., two first FT peaks in Fig. 8), calculated with FEFF ver. 7 functions (Ankudinov and Rehr, 1997), are 2.03 and 2.87 Å for 50GCC, 2.03 and 2.89 Å for NiTcBi, and 2.04–2.05 and 2.90–2.91 Å for NiLit. The Ni–Mn(E) distance in 50GCC is similar to the Mn^{4+}–Mn^{4+} edge-sharing distance in dBi (Villalobos et al., 2006), consistent with an isomorphic substitution of Ni for Mn in the layer of a phyllomanganate (E site) and the multiple chain of a tectomanganate (Fig. 1). For comparison, the Ni–Mn(TC) distance of the interlayer site above an octahedral vacancy (TC site) is 3.48–3.50 Å, and the EXAFS spectra of model compounds in which almost all of the Ni is in the interlayer (NidBi11-4), and 55% in the interlayer and 45% in the layer (NidBi2-7) are much different from 50GCC (Fig. 7).

Based on TEM–EDS data, a portion of Ni in the bulk sample is in the todorokite. In this mineral, Ni is believed to be located in the Mn sites at the edges of the triple chains (Fig. 1, Post and Bish, 1988). At this position, Ni is surrounded by four edge-sharing Mn octahedra at about 2.87–2.91 Å ($\sim$E site), and four corner-sharing Mn octahedra at about 3.48–3.50 Å ($\sim$TC site). Therefore, the Ni todorokite species should appear on the Fourier transform of 50GCC as a Mn peak at $R + \Delta R \approx 3.2$ Å ($\Delta R \sim -0.3$ Å). The overlay plots of the FT of 50GCC with those of NidBi11-4 and NidBi2-7 verify that the three functions have the same signature in the 3.0–3.5 $R + \Delta R$ interval, which suggests that the Ni todorokite species occurs in 50GCC (Fig. 8). The NiBaik reference, which has no todorokite (Manceau et al., 2007b), also has a peak in this region, but its maximum is shifted by 0.1 Å. The average number of corner-sharing Mn octahedra per Ni atom in 50GCC, and thus the fraction of total Ni in the todorokite component, can be estimated from the height of the Mn(TC) peak relative to those for NidBi11-4 and NidBi2-7. In NidBi11-4, Ni has 6 Mn(TC) neighbors because essentially all of the Ni is in the interlayer, and in NidBi2-7 it has $6 \times 0.55 = 3.3$ Mn neighbors. From the height of the Ni–Mn(TC) peak in 50GCC, N[Mn(TC)] is estimated to 1.7, and the proportion of Ni in todorokite to 1.7/4 = 42%.

This proportion cannot be calculated independently from the proportions of todorokite and phyllomanganate in the sample, as determined by Mn-EXAFS, and from the concentrations of Ni in each mineral species, as determined by microanalysis (Table 2), without knowing the proportions of each of the three mineral species in the sample and their average Ni content. For example, let us assume that the sample has 55% todorokite at 2.45% NiO, and that the 45% of phyllomanganate determined by Mn-EXAFS
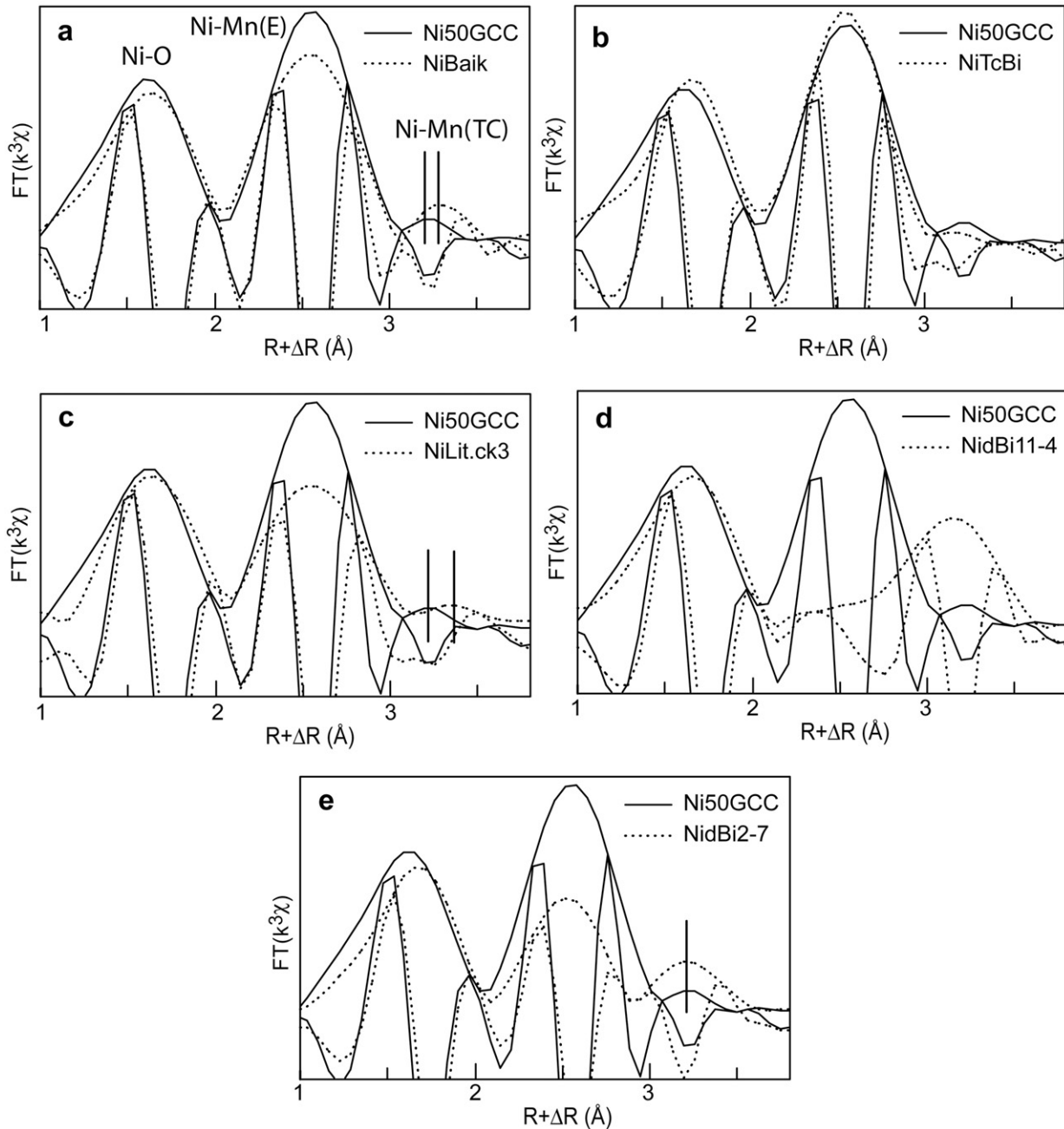
Fig. 8. Fourier transforms (FTs) of the Ni-EXAFS data in Fig. 7.

comprises 40% 10Å-vernadite at 5.01% NiO and 60% 7Å-vernadite at 1.23% NiO. Then the fraction of Ni atoms in each species is 0.52, 0.35 and 0.13, respectively.

Although the percentage of Ni todorokite derived from Ni-EXAFS (42%) cannot be verified, this value can be used to estimate the proportions of 7- and 10Å-vernadite in the sample and, from these values, the fraction of Ni atoms in the two phyllomanganate species. Carrying out the algebra, the fraction of Ni atoms in the three species are

$$y_{todo} = 1.347/(1.90 + 3.78x)$$
$$y_{10Å} = 5.01x/(1.90 + 3.78x)$$
$$y_{7Å} = (0.553 - 1.23x)/(1.90 + 3.78x)$$

where x is the proportion of 10Å-vernadite to total manganate (Fig. 9). Since the proportion of phyllomanganate is 0.45, the proportion of 7Å-vernadite is 0.45-x. We can verify that the vertical line defined by $x = 0.45 * 0.40 = 0.18$ intercepts the three functions at 0.13, 0.35 and 0.52 in (Fig. 9), in agreement with the numerical example. The proportion of 10Å-vernadite is obtained from the intercept of the $y = 0.42$ horizontal line with the y_{todo} function, which equals 0.35. Thus, $y_{10Å} = 0.54$ and $y_{7Å} = 0.04$. Based on this analysis, the sample contains 55% todorokite, 35% 10Å-vernadite and 10% 7Å-vernadite, and nickel is distributed among the three manganates in proportions of 42%, 54% and 4%, respectively. Consequently, 10Å-vernadite is
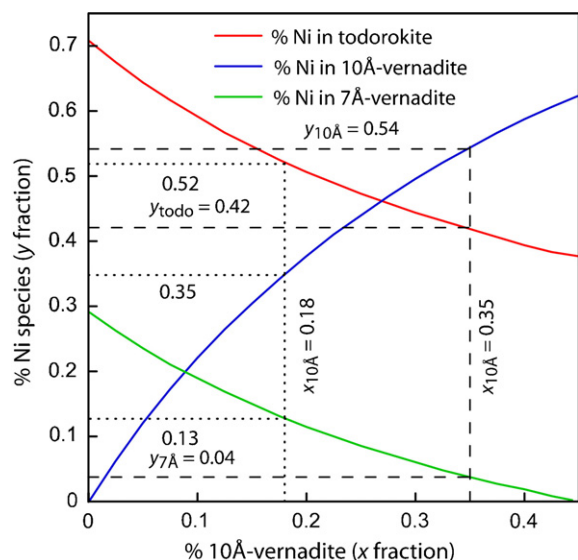
Fig. 9. Ni species—Mineral species graph.

the most Ni-rich phase and also contains the majority of the Ni pool.

Bulk EXAFS spectroscopy is used to quantify metal species in multi-component systems (Manceau et al., 1996, 2002b). According to the current paradigm, only metal species with distinct short range order can be discriminated by this technique, because linear decompositions of multi-component spectra with pure components from similar species leads to multiple solutions. Here, this limitation prevented us from quantifying the fraction of Ni in each phyllomanganate species from EXAFS data alone, so we had to complement the Ni-EXAFS with Mn-EXAFS and TEM–EDS data. By combining microchemical data on phase composition with spectroscopic data on mineral and metal species, it is possible to build metal species - mineral species graphs (Fig. 9) from which an unknown proportion of either species in a complex assemblage can be determined.

4. DISCUSSION

4.1. Mechanism for the transformation of 7- to 10Å-vernadite to todorokite

There are two steps in the synthesis of todorokite (Golden et al., 1986, 1987; Shen et al., 1993; Feng et al., 1995, 2004; Ching et al., 1999; Luo et al., 1999). The first step is the preparation of Na-birnessite (TcBi, $Na_{0.31}(Mn^{4+}_{0.69}Mn^{3+}_{0.31})O_2 \cdot nH_2O$, Silvester et al., 1997; Lanson et al., 2002b) followed by its transformation to buserite (i.e., 10Å-birnessite) by exchanging Na with a cation that retains its full hydration sphere in the interlayer. Inserting a second layer of water in birnessite expands the interlayer from ~5 to ~8 Å and allows its pillaring by triple chains of edge-shared MnO_6 octahedra, the future walls of the todorokite framework (Fig. 1, Post and Bish, 1988). Magnesium is generally used as templating ion because it has the highest ionic potential among alkali and alkaline earth cations, and thus the highest affinity for water, and because its hydrated diameter (8.6 Å) matches the 3 × 3

tunnel size (~10Å in diagonal) (Nightingale, 1959; Ferrage et al., 2005). The second step is the aging of Mg-buserite at pH 12–14 and $T \sim 150$–160 °C for one to two days. Since the transformation is topotactic, the quality of todorokite crystals depends on the crystallinity of the layered precursor (Shen et al., 1993). The phyllomanganate precursor and todorokite product synthesized in the laboratory have a number of morphological, physico-chemical and crystallographic similarities to those formed in nature, as shown below.

In both natural and synthetic todorokite, the transformation starts with a c-ordered Mg-rich 10Å-phyllomanganate template. Syntheses performed with turbostratic 10Å-vernadite as precursor instead of buserite, yield a reaction product that is a mixture of primary 7Å-vernadite and jianshuite/Mg-chalcophanite and secondary poorly-crystallized todorokite (Fig. EA-5). Attempts to synthesize todorokite from 7Å-birnessite fail, and instead yield hollandite ($T(2,2)$ tectomanganate), with K, and romanechite ($T(2,3)$ tectomanganate), with Ba (Feng et al., 1998) as the tunnel-templating ions. The structure-directing role of Mg, and its high concentration in seawater relative to Ca which reversely is more abundant in freshwater (Appelo and Postma, 1996; Andersen et al., 2005; Rezaei et al., 2005), explain why todorokite is widespread in marine deposits and seldom present in continental environments, such as soils (Chukhrov and Gorshkov, 1981; Dixon and Skinner, 1992; Vodyanitskii et al., 2004) or surface coatings and concretions formed in freshwater (Manceau et al., 2007a,b). Continental phyllomanganates generally are calcic (Taylor et al., 1964; Glover, 1977; Chukhrov et al., 1980a, 1985b; McKenzie, 1989; Bilinski et al., 2002; Manceau et al., 2007b), and experimental studies have shown that the conversion of Ca-exchanged birnessite to todorokite is incomplete and the products polyphasic (Golden et al., 1987).

The morphology and outward radial increase in crystallinity of the manganese concretion suggest that the three Mn oxides formed successively from the core. Here, we examine the mechanism of this mineralogical differentiation. The greater thickness of the 10Å particles relative to the 7Å particles correlates with a 50% lower Fe content (Table 2). The same correlation was reported in hydrothermal Mn oxides, although for Fe concentrations ten times higher than here (Buatier et al., 2004). A parallel can be made also with soil kaolinites, whose crystallinity is decreased by epitaxial overgrowth of Fe oxide nanoparticles (Boudeulle and Muller, 1988; Muller et al., 1995). Another possible reason for the low crystallinity of 7Å particles is their intimate mixing in the inner pores and cavities of the concretion with colloidal matter, organic and biological debris, and mineral fragments (e.g., Burns and Burns, 1975; Burns and Burns, 1978b; Siegel and Turner, 1983; Buatier et al., 2004). Burns and Burns (1978b) suggested that the low Ni 'amorphous' or cryptocrystalline Mn oxides, here identified as 7Å-vernadite, transform to Ni-rich todorokite in marine nodules as follows. Manganese oxides freshly precipitated at the surface of detrital matter are thermodynamically unstable and would be dissolved by organic carbon, releasing Mn^{2+} into pore waters. Aqueous Mn^{2+} is readsorbed on 7Å-vernadite, which transforms into todorokite. The disso-

lution of biogenic silica or the oxidation of organic matter release nickel, which becomes available for uptake and incorporation into todorokite. This two-step dissolution-recrystallization process proposed by Burns and Burns (1978b) can account for the secondary enrichment of Ni in todorokite measured by electron microprobe, and its low concentration in the first generation of Mn oxides. Our results show that the phyllomanganate to tectomanganate conversion actually is a three-step process, which involves the intermediate formation of semi-ordered 10Å-vernadite crystallites. Both 10Å-vernadite and todorokite are formed *in situ*, and Ni^{2+} is incorporated post-depositionally predominantly in the layers of the phyllomanganate.

The HRTEM results confirm that the two populations of phyllomanganate particles must contain parallel Mn layers separated by about 9 Å for the topotactic transformation to todorokite to take place. Fig. 1 shows that the layers need also to be coherently stacked over several tens of Angströms for the triple octahedral chains to connect two or more successive layers and the electron diffraction data showed that this topologic condition was fulfilled (Fig. 5c). As a result, the *a* and *b* axes of successive layers are oriented in the same directions and, thus, the threefold symmetry of octahedral layers can be preserved during the topotactic transformation. In this case the todorokite crystals are oriented at 120° from one another and stacked in layers, thus forming a platy trilling pattern of matted fibers twinned in the (001) plane (Turner and Buseck, 1981). Here, only two twinning directions at 120° were observed instead of three, possibly as a consequence of the short coherence length of the 10Å crystallites along the *c* direction. Plates with fine-scale hexagonal trillings have been observed in an oceanic nodule, suggesting that the parent 10Å-phyllomanganate crystallites had a high degree of 3D periodicity (Siegel and Turner, 1983; Chukhrov et al., 1985b). Since well-crystallized hexagonal birnessite and buserite are scarce in nature, plates of todorokite fibers twinned in the three equivalent ⟨100⟩ directions should be uncommon.

A semi-ordered 10Å-vernadite parent also accounts for the abundance and intensity of streaks on the electron micrograph of Fig. 5d. The streaking of the diffraction spots in the *a** direction is due to the intergrowth of $T(3,n)$ building blocks with the chain-width disorder parallel to the *a* axis and the tunnel aperture parallel to the *b* axis of the parent phyllomanganate (Fig. 1). This crystallographic orientation is explained in the 10Å-pillaring model by the formation of tunnel walls through the bridging of adjacent layers with triple chains (Post and Bish, 1988). According to this model, the size of the tunnel walls is constant and fixed by the original layer separation, but the size of the ceilings and floors of the tunnels can vary as their width is determined by the separation distance between walls. In this case, building blocks with $n = 2, 3, 4, 5...$ should be equally probable. However, all published diffraction data show that the $T(3,3)$ tunnel size always prevails. The model prediction can be reconciled with diffraction data by considering the structure of the layer. Let us consider, the case of sodium birnessite first and then 10Å-vernadite.

The cell of TcBi is tripled along *a* due to the segregation of Mn atoms in Mn^{4+}-rich and Mn^{3+}-rich rows parallel to *b*, and to the alternation of the Mn chains along *a* according to the sequence Mn^{4+}–Mn^{4+}–Mn^{3+} (Fig. 10, Drits et al., 1997). The kink-like fold of the phyllomanganate layer likely occurs at the Mn^{4+}–O–Mn^{3+} junction because of the elongation of the Mn^{3+}–O bond distance in the *a* direction by the Jahn-Teller distortion (pointed out by vertical dashes in Fig. 10). In decreasing the bond strength of all Mn^{3+} octahedra in this direction, the elongation weakens the structure along the Mn^{3+}-rich rows, and facilitates the folding of the layer in the *b*, or tunnel, direction. The bending of the layer where the Mn^{4+} and Mn^{3+} chains connect, and not the Mn^{4+}–Mn^{4+} chains, implies that the Mn^{3+} cations occupy the sites at the edge of the triple-chains in the todorokite structure, and that the sites in the middle are occupied exclusively by Mn^{4+} cations (Fig. 1). This implication is supported by crystallographic data (Post and Bish, 1988). When sodium is exchanged with Sr^{2+} in TcBi, the distribution of interlayer species (Sr^{2+} and H_2O) is modeled on the distribution pattern of Mn^{4+} and Mn^{3+} in the layer (Fig. 10 of Drits et al., 1997). The *xy* coordinates of the interlayer species are unknown, but if Sr^{2+} sits atop a Mn^{4+} position, then all Sr^{2+} cations are in the middle of the tunnel when the manganate layer is folded along the Mn^{3+}-rich rows to give the todorokite structure. Magnesium may have the same ordered distribution pattern as Sr in the interlayer and, consequently, the two-dimensional arrangement of Mg atoms presumably acts as an additional structure-directing template for the topotactic transformation (Fig. 10).

Any departure from the superstructure of birnessite should induce a modification of the tunnel width along *a*. The less ordered the Mn atoms, the more incoherent the tunnel width should be. This assumption is supported by the following observations. In the study by Duncan et al. (1998), X-ray and electron diffraction and TEM imaging of the birnessite precursor showed that the crystallites were well crystallized both parallel and perpendicular to the layer plane, but that the Mn cations lacked long-range ordering. The todorokite crystallites were twinned in projection along the *c* direction and highly defective in the *a* direction with tunnel widths ranging from quadrupole to septuple chains, consistent with these observations. In contrast, no twinning and streaking were observed when the initial birnessite contained a high proportion of Mg^{2+} and Mn^{3+} in the layer (Shen et al., 1993). The lack of streaks can be explained by the ordering of Mg^{2+} and Mn^{3+} in the layer plane to minimize the lattice strain (Drits et al., 1997). Also, if the Mn^{3+}/Mg^{2+}-rich rows from successive layers are parallel, then neither birnessite nor todorokite crystals should be twinned. Therefore, todorokite crystals formed from Mn^{3+}-low phyllomanganate crystallites should be defective in the *a* direction. This is the case for all natural todorokites described in the literature, with chain widths ranging from double to ninetuple (Chukhrov et al., 1979a, 1985a; Turner and Buseck, 1981). However, all had more of the triple chains, which, in the absence of Mn^{3+}, can be explained by the templating role of Mg^{2+}.

Mellin and Lei (1993) and Lei (1996) suggested that the *n* numbers of todorokite are predetermined by the redox
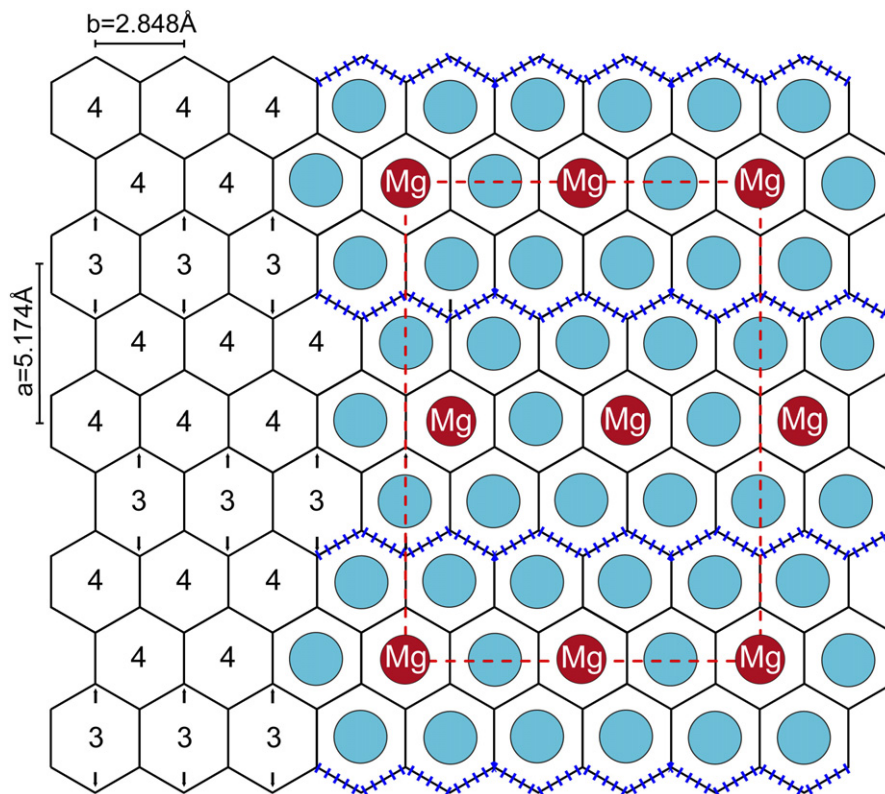
Fig. 10. Distribution of Mn^{3+} and Mn^{4+} in the octahedral layer (left) and possible distribution of Mg and H_2O in the interlayer (right) of Mg-exchanged triclinic birnessite (TcBi). Magnesium is supposed to occupy the same position as Sr (Drits et al., 1997). According to this model, the phyllomanganate layer folds along the corrugated surface delimited by the Mn^{3+}–O–Mn^{4+} weak bonds from the octahedral layer and the HO···H weak bonds from the interlayer. This surface is represented in the *ab* plane by the blue zig-zag line. The tunnels of the todorokite framework are oriented along the Mg–H_2O–Mg chains of the TcBi interlayer. The red dashed line delimits the contours of the $A = 4a$, $B = 4b$ superstructure of Sr-exchanged TcBi observed by electron diffraction (Drits et al., 1997). The structural formula per Mn atom calculated from the supercell is $Mg^{2+}_{0.165}[Mn^{4+}_{0.67} Mn^{3+}_{0.33}]O_2 \cdot 0.83H_2O$. After the topotactic transformation, 50% of the edge sites from the todorokite framework are occupied by Mn^{3+}. The todorokite sample studied by Post et al. (2003) had approximately 40% of those sites occupied by Mn^{3+} (structural formula $Mg^{2+}_{0.07}Na^+_{0.07}Ca^{2+}_{0.02}K^+_{0.02}[Mn^{4+}_{0.73}Mn^{3+}_{0.27}]O_2 \cdot 0.7 H_2O$). In the 50GCC todorokite sample, 25% are occupied by Mn^{3+} and Ni^{2+} (structural formula $Mg^{2+}_{0.08}Ca^{2+}_{0.01}K^+_{0.01}[Mn^{4+}_{0.84} Mn^{3+}_{0.13}Ni^{2+}_{0.03}]O_2 \cdot n H_2O$).

conditions at the time of the phase formation and do not change post-depositionally. This hypothesis conceptually agrees with the structural model presented here. Undefective todorokites ($n = 3$) probably formed from TcBi, that is under conditions in which Mn^{3+} is abundant, whereas highly defective todorokites derive from low Mn^{3+} phyllomanganates. However, there is little potential for the n values to be used as paleoproxies for redox reconstructions because there is no experimental evidence that the dimension of the supercell in the *a* direction increases when the amount of Mn^{3+} decreases. For example, we do not know of birnessites which have 0.25 Mn^{3+} per Mn, and Mn^{3+} rows separated by three Mn^{4+} rows ($T(3,4)$ todorokite structure), nor 0.2 Mn^{3+} per Mn, and Mn^{3+} rows separated by four Mn^{4+} rows ($T(3,5)$ todorokite structure), and so forth.

Since hydrated Mg^{2+} ions are surrounded by four triple-chains in the *ac* plane during the topotactic transformation, is it possible in the absence of Mn^{3+} cations to have enough interlayer Mg^{2+} cations to obtain an undefective $T(3,3)$ structure? In other words, is it possible to crystallize an

undefective todorokite from a Mn^{3+}-free phyllomanganate? We have seen previously with the example of strontium that the required density of interlayer Mg^{2+} cations is ideally one for six Mn atoms since the structural formula of Mg-exchanged TcBi is $Mg_{0.155}(Mn^{4+}_{0.69} Mn^{3+}_{0.31})O_2 \cdot nH_2O$ (Fig. 10). With a layer charge one third lower than that of TcBi (0.22e vs. 0.31e per Mn), the 10Å-vernadite can only yield a defective todorokite. Increasing the layer charge with vacant sites probably is not a solution because this can only happen if the phyllomanganate is equilibrated at low pH (Silvester et al., 1997), and todorokite always is synthesized at alkaline pH. Experimental data suggest that the precursor phyllomanganate should have a low amount of vacancies and a high proportion of substitutional impurities in the layer, which is obtained by co-precipitating a dopant element with Mn during the synthesis of birnessite (Shen et al., 1993; Ching et al., 1999). High charge birnessites have been obtained in this way. These structural considerations lead to the conclusion that the best precursor to todorokite is a Mg-exchanged phyllomanganate that is vacant-free and substituted with heterovalent cations, such as

Mn^{3+}, Ni^{2+} or Cu^{2+}. If this is correct, then it is unclear why the natural todorokites studied here and by Siegel and Turner (1983) have less Ni than the 10Å-phase precursor. It seems that impurities are necessary to kink the initial layer, but that the resulting todorokite framework then incorporates lower amounts of impurities in the edge sites. For topological reasons, connecting the triple chains and accommodating large tunnel cations, such as hydrated Mg^{2+}, may require the M2 octahedra to be distorted. In this case, the Jahn-Teller Mn^{3+} and Cu^{2+} cations are preferred to Ni^{2+}, as its d^8 electronic configuration yields symmetrical octahedra. This is what the study by Siegel and Turner (1983) suggests since the 10Å-phase contained 3.8% NiO and 2.8% CuO, and the todorokite has only 0.2% NiO, but as much as 1.5% CuO.

A last implication of this work is that todorokite may never precipitate homogeneously in water, but may always be a transformation product from a 10Å-phyllomanganate. If correct, then this finding gives general validity to the widely followed assumption that todorokite in nodules is developed exclusively by early diagenetic process (Halbach et al., 1981; Marchig and Halbach, 1982).

4.2. Manganate mineralogy and environment of deposition

The mineralogy of marine manganese deposits often is used to specify their environment of deposition (Usui et al., 1997). Hydrogenetic Mn deposits consist of Fe-vernadite, an intimate mixture on the nanoscale of vernadite and feroxyhite (δ-FeOOH) with a typical Mn/Fe ratio of 1.0 to 1.2 (Manceau and Combes, 1988; Varentsov et al., 1991; Manceau et al., 1992; Usui and Ito, 1994). Despite the paucity of its diffraction lines (two hk bands at 2.40–2.45 and 1.41–1.42 Å), Fe-vernadite is identified unambiguously by XRD because it coexists with other manganese minerals only in hydrogenetic deposits that have been transformed post-depositionally. Thus, this nanocomposite phase is a good indicator of hydrogenetic environment. Distinguishing diagenetic from hydrothermal environments using the mineralogy of Mn oxides is less conclusive because they both contain todorokite and 10Å-phyllomanganate (e.g., Yoshikawa, 1991; Usui et al., 1997; Takahashi et al., 2007). However, 10Å-phyllomanganate tends to prevail in diagenetic deposits, and todorokite in hydrothermal deposits, making a distinction possible when one of the two phases is overwhelmingly present in a sample. Here, this mineralogical signature does not exist because 50GCC contains similar amounts of the two 10Å manganates.

The frequent mixing of todorokite and phyllomanganate has been interpreted as the existence of two structural series: one extending continuously from collapsable 10Å-phyllomanganate ($T(3, \infty)$) to todorokite ($T(3,3)$), and another comprising 10Å-phyllomanganates with different degrees of collapsibility (Usui et al., 1989). The first series occurs in hydrothermal and the second in diagenetic deposits. Variations in layer expandability most likely reflect variations in composition. Layer particles whose interlayer cations have a low enthalpy of hydration, such as K (79 kcal/mol) and Na (97 kcal/mol), collapse in air, while those that are rich in Mg (450 kcal/mol) retain two layers

of water in air (Nightingale, 1959; Ferrage et al., 2005). Particles rich in calcium (373 kcal/mol) have intermediate expandability. Thus, the two genetic manganate series can be viewed alternatively as varying mixtures of todorokite with monovalent-rich (i.e., 7Å) and divalent-rich (i.e., 10Å) phyllomanganate particles. The predominance of todorokite in hydrothermal samples can be explained by the increase of the kinetics of the 10Å-phyllomanganate to todorokite transformation with temperature. Therefore, the three-step solid phase transformation described in this study is probably a common post-depositional process, which occurs during the diagenesis of hydrogeneous and low-temperature hydrothermal deposits.

APPENDIX A. SUPPLEMENTARY DATA

Supplementary data associated with this article can be found in the online version at doi:10.1016/j.gca.2007.07.020.

REFERENCES

Andersen M. S., Nyvang V., Jakobsen R. and Postma D. (2005) Geochemical processes and solute transport at the seawater freshwater interface of a sandy aquifer. *Geochim. Cosmochim. Acta* **69**, 3979–3994.

Ankudinov A. L. and Rehr J. J. (1997) Relativistic calculations of spin-dependent X-ray-absorption spectra. *Phys. Rev. B* **56**, 1712–1716.

Appelo C. A. J. and Postma D. (1996) From rainwater to groundwater. In *Geochemistry, Groundwater and Pollution* (ed. A. A. Balkema). Rotterdam, Brookfield.

Banerjee R., Roy S., Dasgupta S., Mukhopadhyay S. and Miura H. (1999) Petrogenesis of ferromanganese nodules from east of the Chagos Archipelago, Central Indian Basin, Indian Ocean. *Mar. Geol.* **157**, 145–158.

Bilinski H., Giovanoli R., Usui A. and Hanzel D. (2002) Characterization of Mn oxides in cemented streambed crusts from Pinal Creek, Arizona, USA, and in hot-spring deposits from Yuno-Taki falls, Hokkaido, Japan. *Am. Mineral.* **87**, 580–591.

Bonatti E., Zerbi M. R. and Rydell H. S. (1976) Metalliferous deposits from the Apennine ophiolites: Mesozoic equivalents of modern deposits from oceanic spreading centres. *Geol. Soc. Am. Bull.* **87**, 83–94.

Boudeulle M. and Muller J. P. (1988) Structural characteristics of hematite and goethite and their relationships with kaolinite in a

laterite from Cameroon. A TEM study. *Bull. Minéral.* **111**, 149–166.

Buatier M. D., Guillaume D., Wheat C. G., Hervé L. and Adatte T. (2004) Mineralogical characterization and genesis of hydrothermal Mn oxides from the flank of the Juan the Fuca Ridge. *Am. Mineral.* **89**, 1807–1815.

Burns R. G. and Burns V. M. (1975) Mechanism for nucleation and growth of manganese nodules. *Nature* **255**, 130–131.

Burns R. G. and Burns V. M. (1977) The mineralogy and crystal chemistry of deep-sea manganese nodules—a polymetallic resource of the twenty-first century. *Phil. Trans. R. Soc. Lond.* **A286**, 283–301.

Burns V. M. and Burns R. G. (1978a) Authigenic todorokite and phillipsite inside deep-sea manganese nodules. *Am. Mineral.* **63**, 827–831.

Burns V. M. and Burns R. G. (1978b) Post-depositional metal enrichment processes inside manganese nodules from the north equatorial Pacific. *Earth Planet. Sci. Lett.* **39**, 341–348.

Burns R. G. and Burns V. M. (1979) Manganese oxides. In *Marine Minerals* (ed. R. G. Burns). Mineralogical Society of America.

Ching S., Krukowska K. S. and Suib S. L. (1999) A new synthetic route to todorokite-type manganese oxides. *Inorg. Chim. Acta* **294**, 123–132.

Chukhrov F. V., Gorshkov A., Sivtsov A. V. and Berezovskaya V. V. (1979a) New data on natural todorokites. *Nature* **278**, 631–632.

Chukhrov F. V., Gorshkov A. I., Berezovskaya V. V. and Sivtsov A. V. (1979b) Contribution to the mineralogy and authigenic manganese phases from marine manganese deposits. *Miner. Deposita* **14**, 249–261.

Chukhrov F. V., Gorshkov A. I., Rudnitskaya Y. S., Berezovskaya V. V. and Sivtsov A. V. (1980a) Manganese minerals in clays: a review. *Clays Clay Miner.* **28**, 154–346.

Chukhrov F. V., Gorshkov A. I., Vitovskaya I. V., Drits V. A., Sivtsov A. I. and Dikov Y. P. (1980b) Crystallochemical nature of Ni asbolan. *Izvestia Akademia Nauk, SSSR, Ser. Geol.* **9**, 108–120.

Chukhrov F. V., Gorshkov A. I., Vitovskaya I. V., Drits V. A., Sivtsov A. V. and Rudnitskaya E. S. (1980c) Crystallochemical nature of Co–Ni asbolan. *Izvestia Akademia Nauk, SSSR, Ser. Geol.* **6**, 73–81 (Translated in International Geological Review 24, 598–604, 1982).

Chukhrov F. V. and Gorshkov A. I. (1981) Iron and manganese oxide minerals in soils. *Trans. R. Soc. Edinb.* **72**, 195–200.

Chukhrov F. V., Gorshkov A. I., Drits V. A. and Dikov Y. P. (1985a) Structural varieties of todorokite. *Int. Geol. Rev.* **27**, 1481–1491.

Chukhrov F. V., Sakharov B. A., Gorshkov A. I., Drits V. A. and Dikov Y. P. (1985b) Crystal structure of birnessite from the Pacific Ocean. *Int. Geol. Rev.* **27**, 1082–1088 (translated from Investiya Akademie Nauk, SSSR, Seriya Geologicheskaya, 8, 66–73) 27, 1082–1088.

Chukhrov F. V., Drits V. A., Gorshkov A. I., Sakharov B. A. and Dikov Y. P. (1987) Structural models for vernadite. *Int. Geol. Rev.* **29**, 1337–1347.

Cliff G. and Lorimer W. G. (1975) The quantitative analysis of thin specimens. *J. Microsc.* **103**, 203–207.

Corliss J. B., Lyle M., Dymond J. and Crane K. (1978) The geochemistry of hydrothermal mounds near the Galapagos rift. *Earth Planet. Sci. Lett.* **40**, 12–24.

Cronan D. S. (1974) Authigenic minerals in deep-sea sediments. In *The Sea* (ed. E. D. Goldberg). Columbia University, Wiley-Interscience, Palisades, N.Y.

Cronan D. S. and Hodkinson R. A. (1997) Geochemistry of hydrothermal sediments from ODP Sites 834 and 835 in the Lau Basin, southwest Pacific. *Mar. Geol.* **141**, 237–268.

Dixon J. B. and Skinner H. C. W. (1992) Manganese minerals in surface environments. In *Biomineralization Processes of Iron and Manganese. Modern and Ancient Environments* (eds. H. C. W. Skinner and R. W. Fitzpatrick). CATENA Verlag, Cremlingen-Destedt, Germany.

Drits V. A., Silvester E., Gorshkov A. I. and Manceau A. (1997) The structure of synthetic monoclinic Na-rich birnessite and hexagonal birnessite. Part 1. Results from X-ray diffraction and selected area electron diffraction. *Am. Mineral.* **82**, 946–961.

Drits V. A., Lanson B., Bougerol-Chaillout C., Gorshkov A. I. and Manceau A. (2002) Structure of heavy metal sorbed birnessite. Part 2. Results from electron diffraction. *Am. Mineral.* **87**, 1646–1661.

Duncan M. J., Leroux F., Corbett J. M. and Nazar L. F. (1998) Todorokite as a Li insertion cathode—comparison of a large tunnel framework''MnO₂'' structure with its related layered structures. *J. Electrochem. Soc.* **145**, 3746–3757.

Elderfield H. and Greaves M. J. (1981) Negative Cerium anomalies in the rare earth element patterns of oceanographic ferromanganese nodules. *Earth Planet. Sci. Lett.* **55**, 163–170.

Elsass F., Beaumont A., Pernes M., Jaunet A. M. and Tessier D. (1998) Changes in layer organization of Na and Ca exchanged smectite during solvent exchange for embedment in resin. *Can. Mineral.* **36**, 1325–1333.

Feng Q., Kanoh H., Miyai Y. and Ooi K. (1995) Metal ion extraction/insertion reactions with todorokite-type manganese oxide in the aqueous phase. *Chem. Mater.* **7**, 1722–1727.

Feng Q., Yanagisawa K. and Yamasaki N. (1998) Hydrothermal soft chemical process for synthesis of manganese oxides with tunnel structures. *J. Porous Mat.* **5**, 153–161.

Feng X. H., Tan W. F., Liu F., Wang J. B. and Ruan H. D. (2004) Synthesis of todorokite at atmospheric pressure. *Chem. Mater.* **16**, 4330–4336.

Ferrage E., Lanson B., Sakharov B. A. and Drits V. A. (2005) Investigation of smectite hydration properties by modeling experimental X-ray diffraction patterns: Part I. Montmorillonite hydration properties. *Am. Mineral.* **90**, 1358–1374.

Fisher A. T., Stein C. A., Harris R. N., Wang K., Silver E. A., Pfender M., Hutnak M., Cherkaoui A., Bodzin R. and Villinger H. (2003) Abrupt thermal transition reveals hydrothermal boundary and role of seamounts within the Cocos Plate. *Geophys. Res. Lett.* **30**, 1–4.

Gaillot A. C., Flot D., Drits V. A., Burghammer M., Manceau A. and Lanson B. (2003) Structure of synthetic K-rich birnessites obtained by high-temperature decomposition of KMnO₄. I. Two-layer polytype from a 800 °C experiment. *Chem. Mater.* **15**, 4666–4678.

German C. R., Klinkhammer G. P., Edmond J. E., Mitra A. and Elderfield H. (1990) Hydrothermal scavenging of rare-earth elements in the ocean. *Nature* **345**, 516–518.

German C. R., Campbell A. C. and Edmond J. M. (1991) Hydrothermal scavenging at the Mid-Atlantic ridge: modification of trace element dissolved fluxes. *Earth Planet. Sci. Lett.* **107**, 101–114.

Giovanoli R. and Bürki P. (1975) Comparison of X-ray evidence of marine manganese nodules and non-marine manganese ore deposits. *Chimia* **29**, 266–269.

Giovanoli R., Bürki P., Giuffredi S. and Stumm W. (1975) Layer structured manganese oxide hydroxides. IV: the buserite groups; structure stabilization of transition elements. *Chimia* **29**, 517–520.

Glasby G. P. (2006) Manganese: predominant role of nodules and crusts. In *Marine Geochemistry* (eds. H. D. Schulz and M. Zabel). Springer, pp. 371–427.

Glover E. D. (1977) Characterization of marine birnessite. *Am. Mineral.* **62**, 278–285.

Golden D. C., Chen C. C. and Dixon J. B. (1986) Synthesis of todorokite. *Science* **231**, 717–719.

Golden D. C., Chen C. C. and Dixon J. B. (1987) Transformation of birnessite to buserite, todorokite, and manganite under mild hydrothermal treatment. *Clays Clay Miner.* **35**, 271–280.

Golden D. C., Chen C. C., Dixon J. B. and Tokashki Y. (1988) Pseudomorphic replacement of manganese oxides by iron oxide minerals. *Geoderma* **42**, 199–211.

Gutzmer J. and Beukes N. J. (2000) Asbestiform manjiroite and todorokite from the Kalahari manganese field, South Africa. *S. Afr. J. Geol.* **103**, 163–174.

Halbach P., Ozkara M. and Hense J. (1975) The influence of metal content on the physical and mineralogical properties of pelagic manganese nodules. *Miner. Deposita* **10**, 397–411.

Halbach P., Scherhag C., Hebisch U. and Marchig V. (1981) Geochemical and mineralogical control of different genetic types of deep-sea nodules from the Pacific Ocean. *Miner. Deposita* **16**, 59–64.

Hammersley A. P., Svensson S. O., Han M., Fitch A. N. and Hausermann D. (1996) Two-dimensional detector software: from real detector to idealised image or two-theta scan. *High Pressure Res.* **14**, 235–248.

Harris R. N., Fisher A. T. and Chapman D. S. (2004) Fluid flow through seamounts and implications for global mass fluxes. *Geology* **32**, 725–728.

Hatta Y., Watanabe M., Hoshino K. and Usui A. (1999) Comparison of internal structures of marine manganese deposits of hydrogenetic, diagenetic and hydrothermal origins. *Res. Geol.* **49**, 49–54.

Hodkinson R. A., Stoffers P., Scholten J., Cronan D. S., Jeschke G. and Rogers T. D. S. (1994) Geochemistry of hydrothermal manganese deposits from the Pitcairn Island hotspot, southeastern Pacific. *Geochim. Cosmochim. Acta* **58**, 5011–5029.

Holland K. L. and Walker J. R. (1996) Crystal structure modeling of a highly disordered potassium birnessite. *Clays Clay Miner.* **44**, 744–748.

Kuhn T., Bau M., Blum N. and Halbach P. (1998) Origin of negative Ce anomalies in mixed hydrothermal–hydrogenetic Fe–Mn crusts from the Central Indian Ridge. *Earth Planet. Sci. Lett.* **163**, 207–220.

Lanson B., Drits V. A., Silvester E. J. and Manceau A. (2000) Structure of H-exchanged hexagonal birnessite and its mechanism of formation from Na-rich monoclinic buserite at low pH: new data from X-ray diffraction. *Am. Mineral.* **85**, 826–835.

Lanson B., Drits V. A., Gaillot A. C., Silvester E., Plançon A. and Manceau A. (2002a) Structure of heavy metal sorbed birnessite. Part I. Results from X-ray diffraction. *Am. Mineral.* **87**, 1631–1645.

Lanson B., Drits V. A., Feng Q. and Manceau A. (2002b) Crystal structure determination of synthetic Na-rich birnessite: evidence for a triclinic one-layer cell. *Am. Mineral.* **87**, 1662–1671.

Lei G. and Boström K. (1995) Mineralogical control on transition metal distributions in marine manganese nodules. *Mar. Geol.* **123**, 253–261.

Lei G. B. (1996) Crystal structures and metal uptake capacity of 10 angstrom-manganates: an overview. *Mar. Geol.* **133**, 103–112.

Luo J., Zhang Q. H., Huang A. M., Giraldo O. and Suib S. L. (1999) Double-aging method for preparation of stabilized Na-buserite and transformations to todorokites incorporated with various metals. *Inorg. Chem.* **38**, 6106–6113.

Manceau A., Llorca S. and Calas G. (1987) Crystal chemistry of cobalt and nickel in lithiophorite and asbolane from New Caledonia. *Geochim. Cosmochim. Acta* **51**, 105–113.

Manceau A. and Combes J. M. (1988) Structure of Mn and Fe oxides and oxyhydroxides: a topological approach by EXAFS. *Phys. Chem. Miner.* **15**, 283–295.

Manceau A., Gorshkov A. I. and Drits V. A. (1992) Structural chemistry of Mn, Fe, Co, and Ni in Mn hydrous oxides. II. Information from EXAFS spectroscopy, electron and X-ray diffraction. *Am. Mineral.* **77**, 1144–1157.

Manceau A., Boisset M. C., Sarret G., Hazemann J. L., Mench M., Cambier P. and Prost R. (1996) Direct determination of lead speciation in contaminated soils by EXAFS spectroscopy. *Environ. Sci. Technol.* **30**, 1540–1552.

Manceau A., Drits V. A., Silvester E., Bartoli C. and Lanson B. (1997) Structural mechanism of Co(II) oxidation by the phyllomanganate, Na-buserite. *Am. Mineral.* **82**, 1150–1175.

Manceau A., Lanson B. and Drits V. A. (2002a) Structure of heavy metal sorbed birnessite. Part III. Results from powder and polarized extended X-ray absorption fine structure spectroscopy. *Geochim. Cosmochim. Acta* **66**, 2639–2663.

Manceau A., Marcus M. A. and Tamura N. (2002b) Quantitative speciation of heavy metals in soils and sediments by synchrotron X-ray techniques. In *Applications of Synchrotron Radiation in Low-Temperature Geochemistry and Environmental Science*, 49 (eds. P. A. Fenter, M. L. Rivers, N. C. Sturchio and S. R. Sutton). Springer, pp. 341–428.

Manceau A., Tamura N., Marcus M. A., MacDowell A. A., Celestre R. S., Sublett R. E., Sposito G. and Padmore H. A. (2002c) Deciphering Ni sequestration in soil ferromanganese nodules by combining X-ray fluorescence, absorption and diffraction at micrometer scales of resolution. *Am. Mineral.* **87**, 1494–1499.

Manceau A., Marcus M. A., Tamura N., Proux O., Geoffroy N. and Lanson B. (2004) Natural speciation of Zn at the micrometer scale in a clayey soil using X-ray fluorescence, absorption, and diffraction. *Geochim. Cosmochim. Acta* **68**, 2467–2483.

Manceau A., Tommaseo C., Rihs S., Geoffroy N., Chateigner D., Schlegel M., Tisserand D., Marcus M. A., Tamura N. and Chen Z. S. (2005) Natural speciation of Mn, Ni and Zn at the micrometer scale in a clayey paddy soil using X-ray fluorescence, absorption, and diffraction. *Geochim. Cosmochim. Acta* **69**, 4007–4034.

Manceau A., Lanson M. and Geoffroy N. (2007a) Natural speciation of Ni, Zn, Ba and As in ferromanganese coatings on quartz using X-ray fluorescence, absorption, and diffraction. *Geochim. Cosmochim. Acta* **71**, 95–128.

Manceau A., Kersten M., Marcus M. A., Geoffroy N. and Granina L. (2007b) Ba and Ni speciation in a nodule of binary Mn oxide phase composition from Lake Baikal. *Geochim. Cosmochim. Acta* **71**, 1967–1981.

Marchig V. and Halbach P. (1982) Internal structures of manganese nodules related to conditions of sedimentation. *Tschermaks. Mineral. Petrogr. Mitt.* **30**, 81–110.

Marcus M. A., MacDowell A. A., Celestre R., Manceau A., Miller T., Padmore H. A. and Sublett R. E. (2004a) Beamline 10.3.2 at ALS: a hard X-ray microprobe for environmental and materials sciences. *J. Synch. Rad.* **11**, 239–247.

Marcus M. A., Manceau A. and Kersten M. (2004b) Mn, Fe, Zn and As speciation in a fast-growing ferromanganese marine nodule. *Geochim. Cosmochim. Acta* **68**, 3125–3136.

Matocha C. J., Elzinga E. J. and Sparks D. L. (2001) Reactivity of Pb(II) at the Mn(III,IV) (oxyhydr)oxide-water interface. *Environ. Sci. Technol.* **35**, 2967–2972.

McCoy F. W. and Sancetta C. (1985) North Pacific sediments. In *The Ocean Basins and Margins* (eds. A. E. M. Naim, F. G. Stehli and S. Uyeda). Plenum Press, New York.

McKenzie R. M. (1989) Manganese oxides and hydroxides. In *Minerals in Soil Environments* (eds. J. B. Dixon and S. B. Weed). Soil Science Society of America, Madison, Madison, WI.

McKeown D. A. and Post J. E. (2001) Characterization of manganese oxide mineralogy in rock varnish and dendrites using X-ray absorption spectroscopy. *Am. Mineral.* **86**, 701–713.

McLennan S. M. (1989) Rare earth elements in sedimentary rocks: influence of provenance and sedimentary processes. *Rev. Mineral.* **21**, 169–200.

Mellin T. and Lei G. (1993) Stabilization of 10Å-manganates by interlayer cations and hydrothermal treatment: implications for the mineralogy of marine manganese concretions. *Mar. Geol.* **115**, 67–83.

Moore W. S., Ku T. L., Macdougall J. D., Burns V. M., Burns R. G., Dymond J., Lyle M. and Piper D. Z. (1981) Fluxes of metals to a manganese nodule: radiochemical, chemical, structural and mineralogical studies. *Earth Planet. Sci. Lett.* **52**, 151–171.

Morin G., Ostergren J. D., Juillot F., Ildefonse P., Calas G. and Brown G. E. J. (1999) XAFS determination of the chemical form of lead in smelter-contaminated soils and mine tailings: importance of adsorption processes. *Am. Mineral.* **84**, 420–434.

Morin G., Juillot F., Ildefonse P., Calas G., Samama J. C., Chevallier P. and Brown G. E. (2001) Mineralogy of lead in a soil developed on a Pb-mineralized sandstone (Largentière, France). *Am. Mineral.* **86**, 92–104.

Muller J. P., Manceau A., Calas G., Allard T., Ildefonse P. and Hazemann J. L. (1995) Crystal chemistry of kaolinite and Fe–Mn oxides: relation with formation conditions of low temperature systems. *Am. J. Sci.* **295**, 1115–1155.

Nightingale E. R. (1959) Phenomenological theory of ion solution. Effective radii of hydrated ions. *J. Phys. Chem.* **63**, 1381–1387.

Ostwald J. (1984) Ferruginous vernadite in an Indian ocean ferromanganese nodule. *Geol. Mag.* **121**, 483–488.

Piepgras D. J. and Jacobsen S. B. (1992) The behavior of rare earth elements in seawater: precise determination of variations in the North Pacific water column. *Geochim. Cosmochim. Acta* **56**, 1851–1862.

Post J. E. and Appleman D. E. (1994) Crystal structure refinement of lithiophorite. *Am. Mineral.* **79**, 370–374.

Post J. E. and Bish D. L. (1988) Rietveld refinement of the todorokite structure. *Am. Mineral.* **73**, 861–869.

Post J. E., Heaney P. J. and Hanson J. (2003) Synchrotron X-ray diffraction of the structure and dehydration behavior of todorokite. *Am. Mineral.* **88**, 142–150.

Proux O., Nassif V., Prat A., Ulrich O., Lahera E., Biquard X., Menthonnex J. J. and Hazemann J. L. (2006) Feedback system of a liquid-nitrogen-cooled double-crystal monochromator: design and performances. *J. Synch. Rad.* **13**, 59–68.

Rezaei M., Sanz E., Raeisi E., Ayora C., Vazquez-sune E. and Carrera J. (2005) Reactive transport modeling of calcite dissolution in the fresh-salt water mixing zone. *J. Hydrol.* **311**, 282–298.

Riley J. P. and Chester R. (1971) *Introduction to Marine Chemistry*. Academic Press, London.

Samuel J., Rouault R. and Besnus Y. (1985) Analyse multiélémentaire standardisée des matériaux géologiques en spectrométrie d'émission par plama par couplage inductif. *Analusis* **13**, 312–317.

Shen Y. F., Zerger R. P., Deguzman R. N., Suib S. L., Mccurdy L., Potter D. I. and Oyoung C. L. (1993) Manganese oxide octahedral molecular sieves—preparation, characterization, and applications. *Science* **260**, 511–515.

Siegel M. D. and Turner S. (1983) Crystalline todorokite associated with biogenic debris in manganese nodules. *Science* **219**, 172–174.

Silvester E., Manceau A. and Drits V. A. (1997) The structure of synthetic monoclinic Na-rich birnessite and hexagonal birnessite. Part 2. Results from chemical studies and EXAFS spectroscopy. *Am. Mineral.* **82**, 962–978.

Takahashi Y., Manceau A., Geoffroy N., Marcus M. A. and Usui A. (2007) Chemical and structural control of the partitioning of Co, Ce, and Pb in marine ferromanganese oxides. *Geochim. Cosmochim. Acta* **71**, 984–1008.

Taylor R. M., McKenzie R. M. and Norrish K. (1964) The mineralogy and chemistry of manganese in some Australian soils. *Aust. J. Soil Res.* **2**, 235–248.

Teo B. K. (1986) *EXAFS: Basic Principles and Data Analysis.* Springer-Verlag, Berlin.

Turner S. and Buseck P. R. (1979) Manganese oxide tunnel structures and their intergrowths. *Science* **203**, 456–458.

Turner S. and Buseck P. R. (1981) Todorokites: a new family of naturally occurring manganese oxides. *Science*, 1024–1027.

Turner S., Siegel M. D. and Buseck P. R. (1982) Structural features of todorokite intergrowths in manganese nodules. *Nature* **296**, 841–842.

Usui A. (1979) Nickel and copper accumulations as essential elements in 10-Å manganite of deep-sea manganese nodules. *Nature* **279**, 411–413.

Usui A., Yuasa M., Yokota M., Nishimura A. and Murakami M. F. (1986) Submarine hydrothermal manganese deposits from the Ogasawara (Bonin) Arc, off the Japan Islands. *Mar. Geol.* **73**, 311–322.

Usui A., Mellin T. A., Nohara M. and Yuasa M. (1989) Structural stability of marine 10Å manganates from the Ogasawara (Bonin) arc: implication for low-temperature hydrothermal activity. *Mar. Geol.* **86**, 41–56.

Usui A. and Nishimura A. (1992) Submersible observations of hydrothermal manganese deposits on the Kaikata Seamount, Izu-Ogasawara (Bonin) Arc. *Mar. Geol.* **106**, 203–216.

Usui A. and Ito T. (1994) Fossils manganese deposits buried within DSDP/ODP cores, Legs 1–126. *Mar. Geol.* **119**, 111–136.

Usui A. and Mita N. (1995) Geochemistry and mineralogy of a modern buserite deposit from a hot spring in Hokkaido, Japan. *Clays Clay Miner.* **43**, 116–127.

Usui A., Bau M. and Yamazaki T. (1997) Manganese microchimneys buried in the Central Pacific pelagic sediments: evidence of intraplate water circulation? *Mar. Geol.* **141**, 269–285.

Usui A. and Glasby G. P. (1998) Submarine hydrothermal manganese deposits in the Izu-Bonin-Mariana arc: an overview. *Isl. Arc* **7**, 422–431.

Varentsov I. M., Drits V. A., Gorshkov A. I., Sivtsov A. V. and Sakharov B. A. (1991) Me–Fe oxyhydroxide crusts from Krylov seamount (Eastern Atlantic): mineralogy, geochemistry and genesis. *Mar. Geol.* **96**, 53–70.

Villalobos M., Bargar J. and Sposito G. (2005) Mechanisms of Pb(II) sorption on a biogenic manganese oxide. *Environ. Sci. Technol.* **39**, 569–576.

Villalobos M., Lanson B., Manceau A., Toner B. and Sposito G. (2006) Structural model for the biogenic Mn oxide produced by *Pseudomonas putida*. *Am. Mineral.* **91**, 489–502.

Vodyanitskii Y. N., Vasilev A. A., Lesovaya S. N., Sataev E. F. and Sivtsov A. V. (2004) Formation of manganese oxides in soils. *Eurasian Soil Sci.* **37**, 572–584.

Wen X., De Carlo E. H. and Li Y. H. (1997) Interelement relationships in ferromanganese crusts from the central Pacific ocean: their implications for crust genesis. *Mar. Geol.* **136**, 277–297.

Yang D. S. and Wang M. K. (2003) Characterization and a fast method for synthesis of sub-micron lithiophorite. *Clays Clay Miner.* **51**, 96–101.

Yoshikawa K. (1991) The relationship between manganese minerals and metallic elements in deep-sea manganese nodules. *Mar. Geol.* **101**, 267–286.

Associate editor: Garrison Sposito

Samples	50GC 12	50GC 26	50GC 30	50GC 38	50GC 54	50GC 58	50GC 70	50GC 100	50GC 110	50GC 124
SiO_2 (%)	48.6	46.0	46.6	45.1	43.2	44.3	43.4	15.1	26.0	25.9
Al_2O_3	16.1	14.7	15.0	14.9	13.7	13.4	13.6	4.7	5.8	5.9
MgO	3.2	3.4	3.4	3.6	3.6	3.7	3.3	3.9	2.7	2.8
CaO	2.0	2.5	2.2	2.6	3.2	2.8	4.4	4.0	22.2	21.9
Fe_2O_3	8.0	7.2	7.2	7.9	6.9	7.0	7.0	2.8	10.1	10.5
MnO	2.6	2.5	2.8	2.8	4.4	5.3	5.2	42.3	5.2	3.8
TiO_2	0.8	0.7	0.7	0.8	0.7	0.7	0.7	0.2	0.3	0.3
Na_2O	4.6	4.6	5.2	5.0	5.4	4.5	4.9	1.5	3.5	3.7
K_2O	2.4	2.6	2.4	2.3	1.9	2.2	2.6	0.3	1.0	1.6
P_2O_5	0.4	0.8	0.7	0.8	1.3	1.2	2.2	1.9	11.7	12.3
LOI	9.4	11.3	10.9	11.5	12.0	11.6	10.8	18.7	13.1	11.2
Sum	98.1	96.2	97.0	97.1	96.3	96.7	98.2	95.3	101.4	99.9
Ni (mg/kg)	519	1 717	543	392	692	743	1 044	6 333	1 924	1 598
Co	44	35	38	42	55	46	64	765	63	58
Cu	400	1 086	340	1 140	432	1 313	1 092	978	289	676

Table EA-1. Concentrations of major (wt. %) and minor (mg/kg) elements along the sediment core. LOI = loss on ignition. All elements were analyzed by ICP-AES. The digits to the right of the sample name is the depth in centimeter. The sample referred to as 50GCC in the article is 50GCC100.
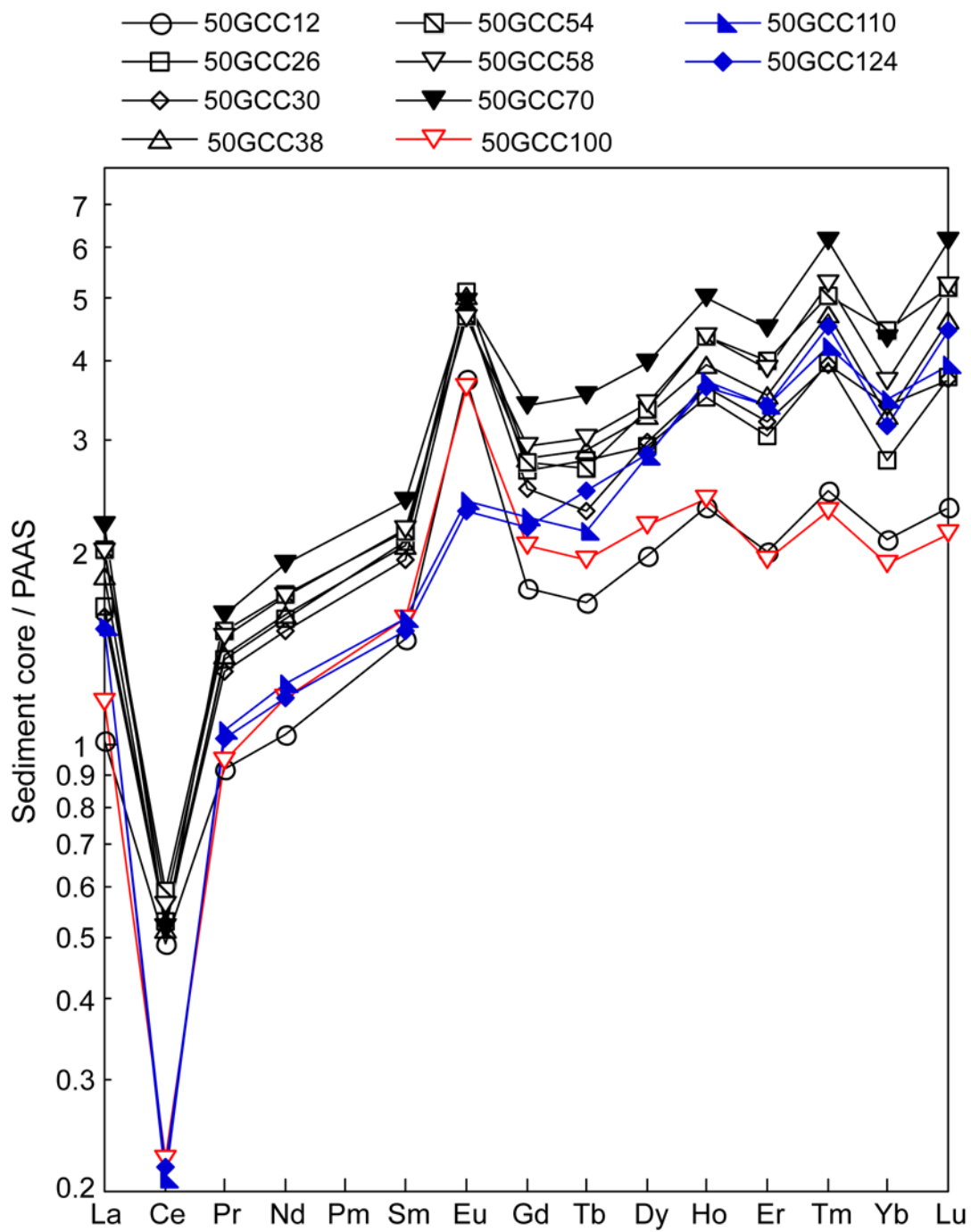
Fig. EA-1. REE patterns normalized to abundances in Post-Archean Australian Shale (PAAS, McLennan, 1989) for the sediment core. The digits to the right of the sample name is the depth in centimeter. The sample referred to as 50GCC in the article is 50GCC100.
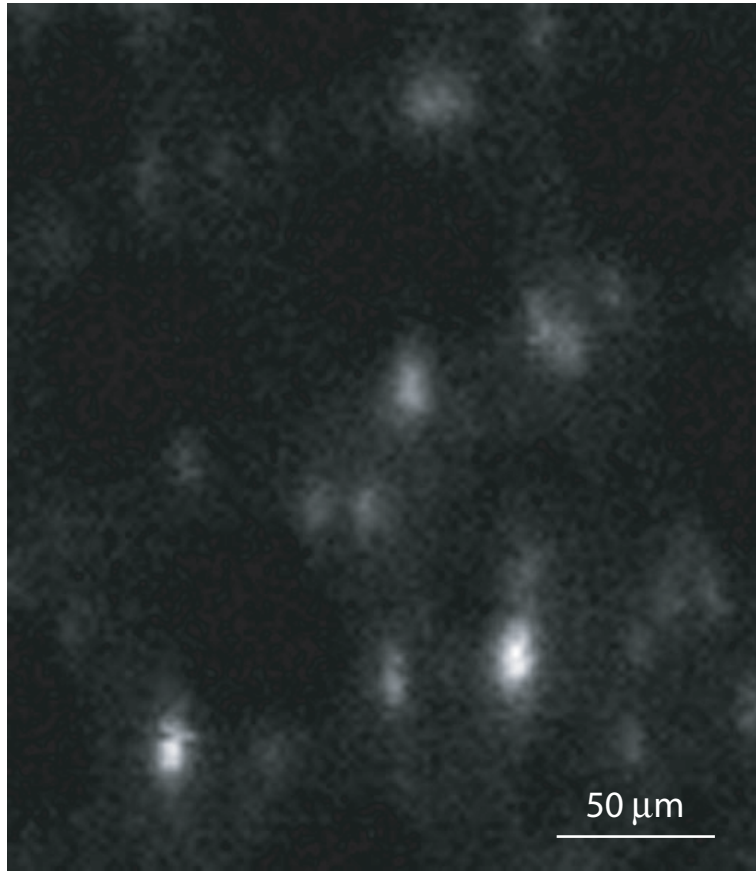
Fig. EA-2. Typical micro X-ray fluorescence map of Ni in a fine powder from the nodule dispersed on a TEM beryllium grid. The map was scanned at 2 x 2 μm^2 resolution with a 5 x 5 μm^2 beam size. Micro XRD data were collected on the center and rim of bright (Ni-rich) particles and on dim (Ni-poor) particles.
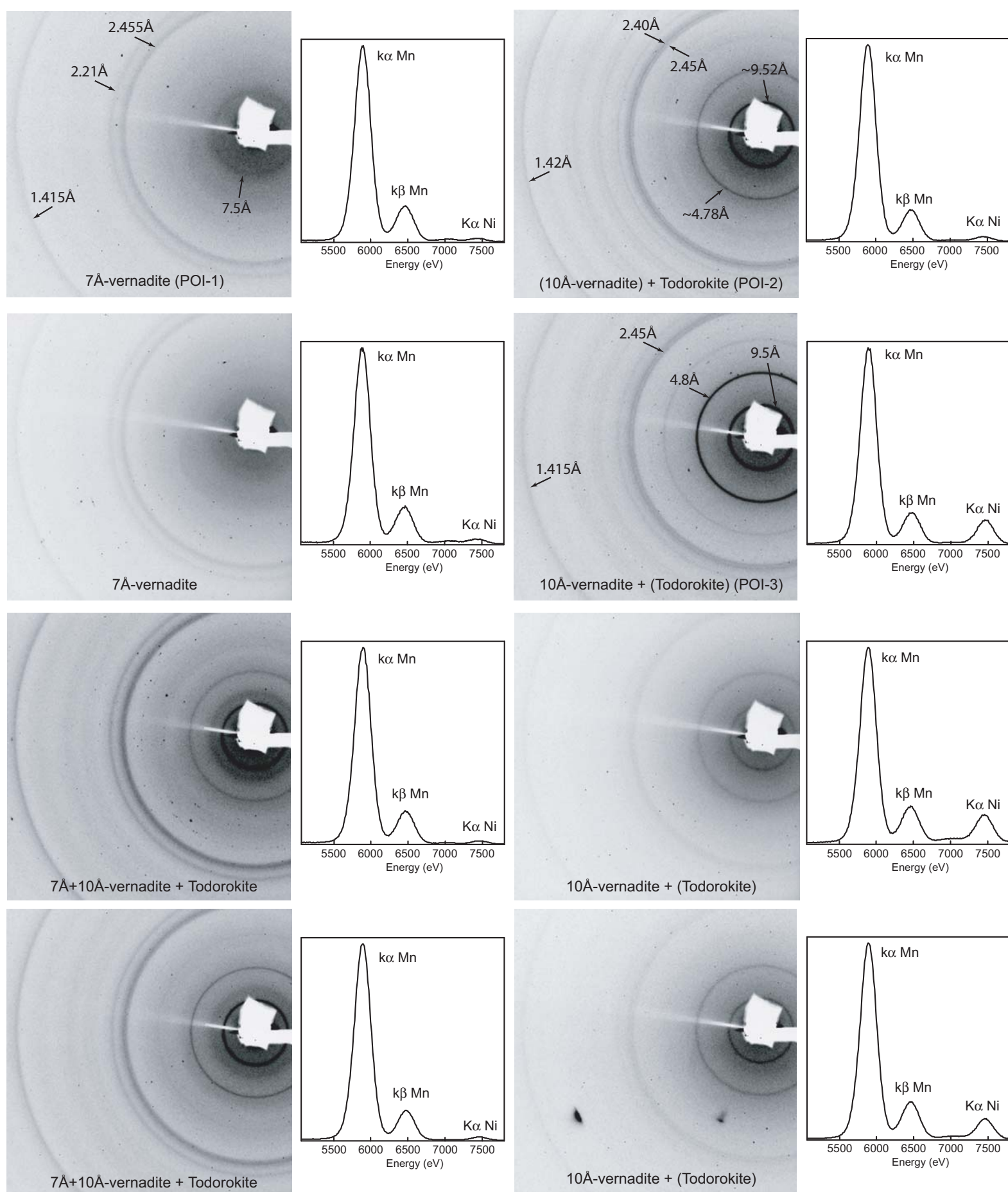
Fig. EA-3. Illustration of the variability of μ-XRF (right) and μ-XRD data (left) collected on Ni-rich and Ni-poor spots from XRF maps, as the one presented in Fig. EA-2. The one-dimensional XRD patterns at POI-1, POI-2 and POI-3 presented in Fig. 3 were obtained by radially integrating and background subtracting the scattered intensity from the 2D patterns.
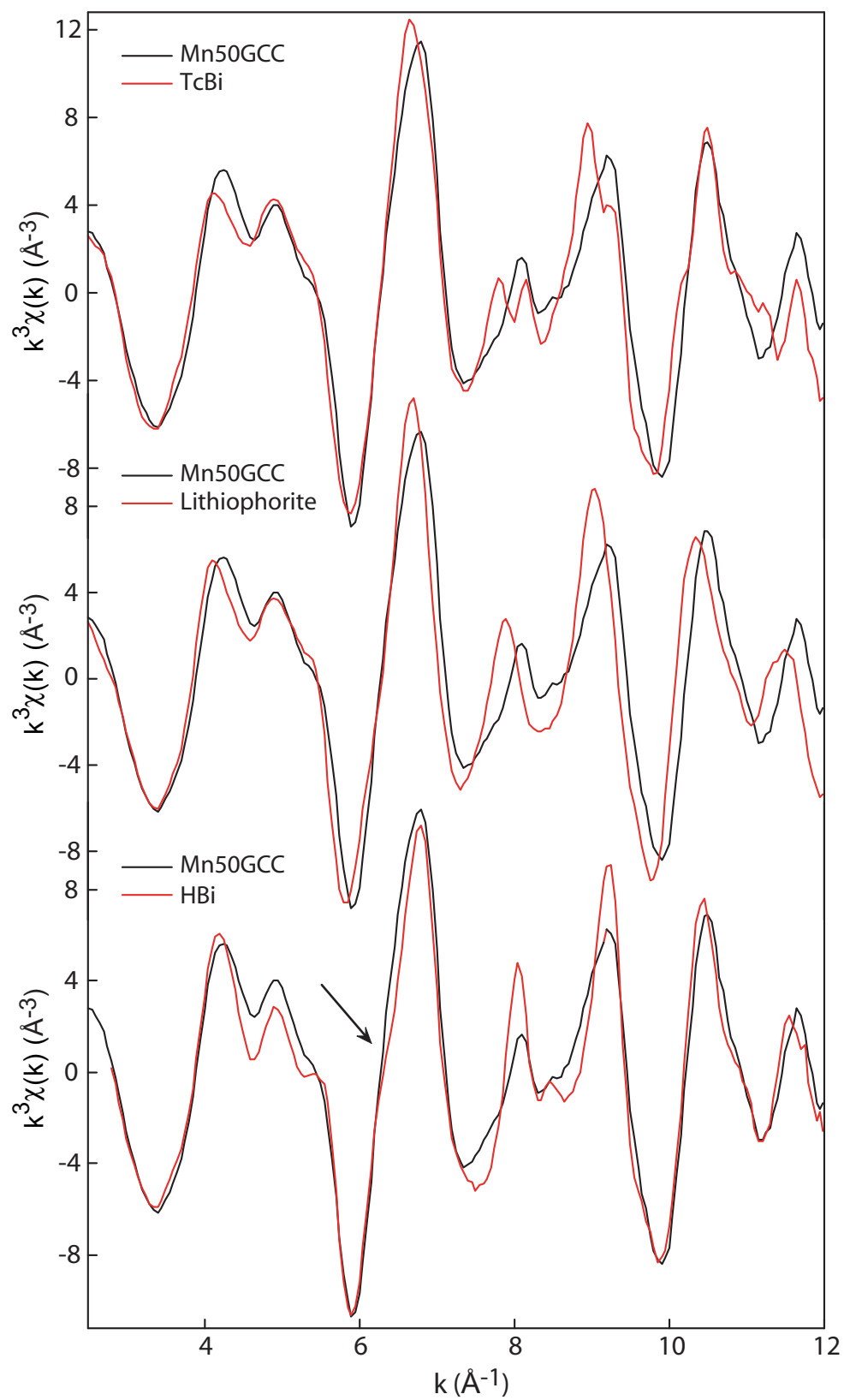
Fig. EA-4. Manganese K-edge EXAFS spectrum of 50GCC compared to three reference spectra. None of the three Mn species describe the data as well as todorokite and dBi (Fig. 4).
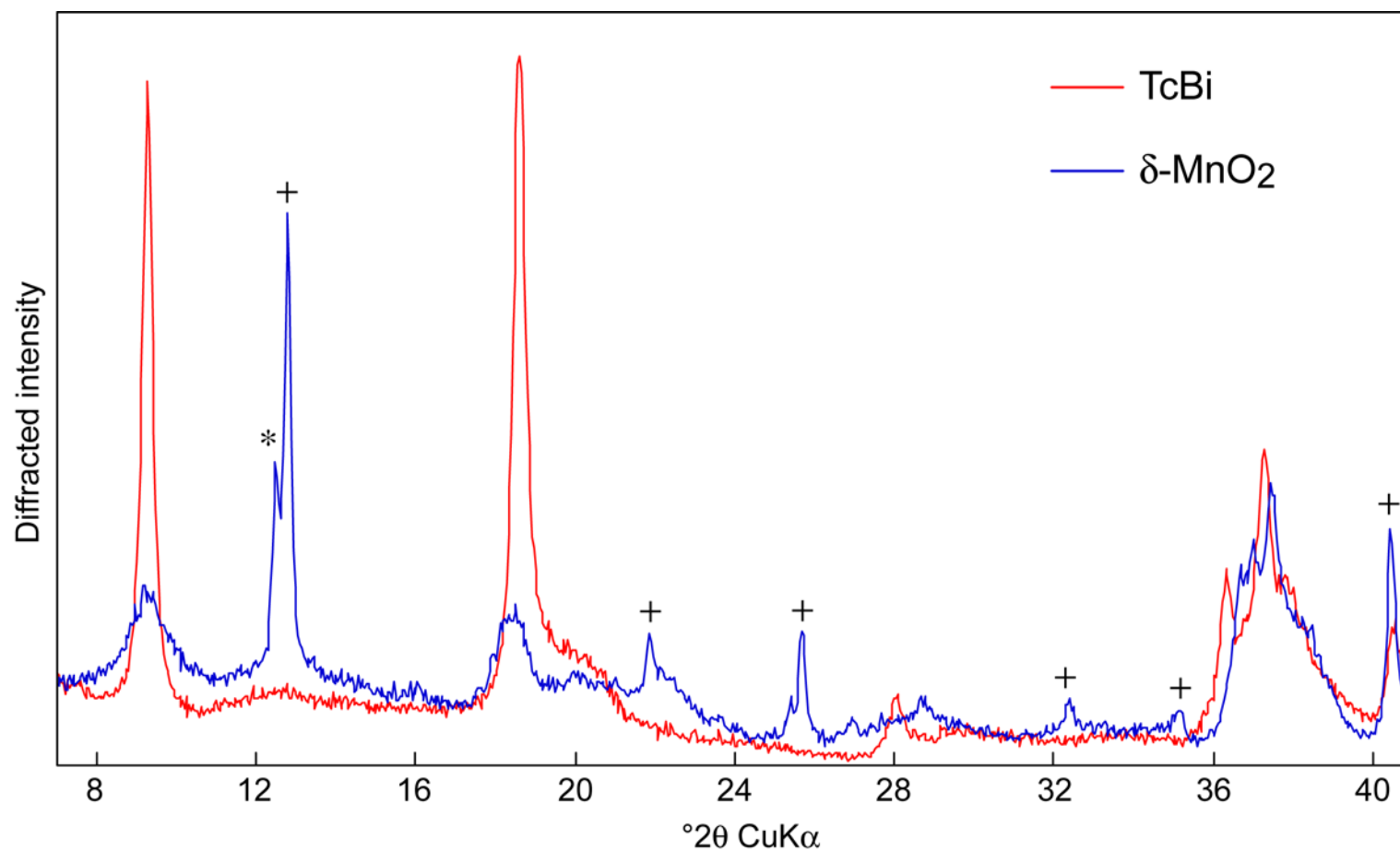
Fig. EA-5. XRD traces of Mg-exchanged triclinic birnessite (TcBi) and synthetic vernadite (δ-MnO$_2$) heated for 24h at 155°C and freeze-dried. TcBi has transformed completely to todorokite. δ-MnO$_2$ has transformed partly to poorly-crystallized todorokite and jianshuite/Mg-chalcophanite (+). * = unreacted δ-MnO$_2$. Data recorded in air.